



Cite this: *Mater. Adv.*, 2022, 3, 5698

## Origin of luminescence properties and synthetic methods for gold- and bimetallic gold-based nanomaterials

Kanika Bharti,† Jitendra K. Sahu† and Kalyan K. Sadhu  \*

Organic emissive dyes, which were first synthesized in the mid-19th century, have played a major role in the field of sensing and biological imaging for several decades. The extensive use of  $\pi$  conjugation in organic dyes has shown their red-shifted emission from the ultraviolet (UV) to near infrared (NIR) region. The emission property modulation is not only restricted to  $\pi$  conjugation, but also affects the rotation of their bonds, functional group modification and intermolecular interactions. The photobleaching property of organic dyes makes it necessary to develop alternative emissive molecules and materials. Among the alternative emissive sources, gold-based nanomaterials showed  $10^{-4}$  to  $10^{-5}$  quantum efficiency for the first time in 1998. The quantum yields of these systems are mostly low except for a few exceptional cases in comparison to organic dyes. However, the high extinction coefficient values of these gold-based nanomaterials overcome the issue of overall brightness. The high stability of gold-based nanomaterials has gained attention in sensing and biological applications. The origin of the emission in these gold-based nanomaterials varies significantly among bimetallic nanoclusters (BMNCs) and metal oxide nanoparticles (NPs). In this review article, we deliberate on the foundation of luminescence properties among gold-based nanomaterials and compare their synthetic methods in detail.

Received 22nd May 2022,  
Accepted 15th June 2022

DOI: 10.1039/d2ma00572g

[rsc.li/materials-advances](http://rsc.li/materials-advances)

### 1. Introduction

The emission property of organic dyes is important for studies on biosensing and bioimaging.<sup>1</sup> Small organic fluorophores

have been widely developed<sup>2</sup> for this purpose since their first synthesis more than 150 years ago.<sup>3</sup> Currently, for the synthesis of novel organic fluorophores, a few important parameters should be considered in terms of their physical properties.<sup>4</sup> Among the photophysical properties, the absorption wavelength maximum ( $\lambda_{\text{abs}}$ ), emission wavelength maximum ( $\lambda_{\text{em}}$ ), molar extinction coefficient ( $\epsilon$ ) and quantum yield ( $\Phi_f$ ) are the four important parameters to be determined. The fluorogenicity of

Department of Chemistry, Indian Institute of Technology Roorkee,  
Roorkee – 247667, Uttarakhand, India. E-mail: [sadhu@cy.iitr.ac.in](mailto:sadhu@cy.iitr.ac.in)

† Both the authors contributed equally in this review.



Kanika Bharti

*Ms Kanika Bharti is currently working as a Senior Research Scholar at the Department of Chemistry in IIT Roorkee. She completed her Undergraduate degree from the University of Delhi in 2015 and Post-graduate degree in Chemistry from IIT Mandi in 2017. Her research interest is mainly focused on developing new synthesis methodologies for gold-based nanomaterials at room temperature and their utilization for biological applications.*



Jitendra K. Sahu

*Jitendra Kumar Sahu is a research scholar (PhD) at the IIT Roorkee. He graduated in Chemistry with honours in 2015 from Stewart Science College under Utkal University, Bhubaneswar, Odisha. Then he completed his MSc in Applied Chemistry from IIT Dhanbad, in 2017 before joining the prominent IIT Roorkee for his PhD in 2018. His current research interest includes nano-bio interfacial chemistry involving gold nanoparticles, nucleic acids, amino acids and peptides.*



the quenched fluorophore is also important for sensing and imaging to avoid the background emission, which is a common artifact in imaging studies.<sup>5</sup> This fluorogenicity in the organic fluorophore is commonly achieved through chemical reactions involving bioanalytes.<sup>6</sup> In a few cases, the chemical reactions are controlled by external light irradiation to achieve a better fluorescence response.<sup>7</sup> A molecular-level correlation between the chemical structure of an organic fluorophore and its photophysical properties has been found to be useful for the molecular design of novel fluorescent bioprobes.<sup>8</sup>

In the last two decades, the use of organic fluorophores with high temporal and spatial resolution in bioimaging experiments has been found to be useful in living systems.<sup>9</sup> However, to avoid strong autofluorescence by biomolecules in the ultraviolet region, a recent review article discussed the importance of the development of NIR fluorophores for bioimaging experiments.<sup>10</sup>

The photoluminescent property of metal nanoclusters is significantly different from that of organic fluorophores (Fig. 1A) and dependent on metal–metal, metal–ligand and ligand–ligand interactions. As shown in Fig. 1B, the metal core and Au(I)–S surface contribute to the luminescent property in nanoclusters. The surface-like excited states are affected by the rotational and vibrational motion in surface ligands, where restricted rotational and vibrational motion decreases the non-radiative relaxation and enhances the fluorescence intensity.<sup>11</sup> However, organic fluorophores with high quantum yields suffer from photobleaching with time and brightness in aqueous medium as two major drawbacks.<sup>12</sup> The brightness of an emissive molecule or material is often defined as  $\epsilon \cdot \Phi_f$ .<sup>13</sup> To overcome these limitations, metal-based NPs are considered an alternative probe.<sup>14</sup> The poor  $\Phi_f$  properties of metal-based NPs are generally balanced with a very high value of  $\epsilon$  to produce brightness. The advantages and disadvantages of organic fluorophores vs. metal-based nanoclusters are summarized in Table 1.<sup>15–18</sup> Hence, recently, review articles and perspectives on metal-based

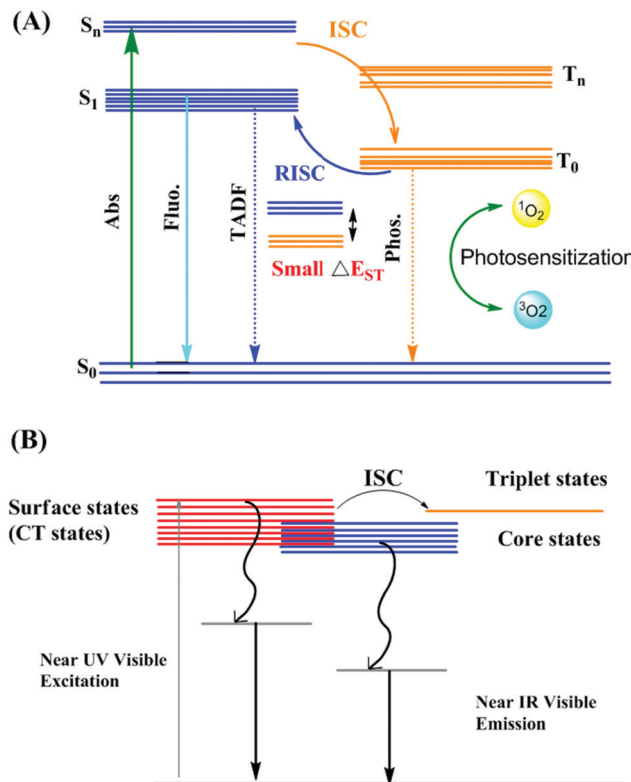


Fig. 1 Schematic Illustration of Jablonski diagram (A) representing photophysical properties and ROS generation mechanism using organic dyes; adapted from ref. 18. (B) Proposed mechanism for the origin of luminescence in metal nanoclusters; adapted from ref. 11.



Dr Kalyan K. Sadhu is currently working as an Associate Professor in Department of Chemistry at IIT Roorkee. In his independent position as an Assistant Professor in the same department, he has started working on nano-bio interfacial chemistry with special emphasis on gold nano- and supra-architectures for biological applications such as imaging, recognition and drug delivery. Prior to this, he was trained in Chemical Biology during his

postdoctoral research stints at the University of Geneva, Switzerland, University of Strasbourg, France and Osaka University, Japan. During his doctoral research at IIT Kanpur, India, he gained research experience in supramolecular chemistry.

Kalyan K. Sadhu

nanomaterials have attracted significant attention for a wide range of applications.<sup>19–28</sup> Among the applications of metal-based NPs, hypoxic tumor radiotherapy is one of the most important for clinical cancer treatment.<sup>19</sup> An integrated “metallomics” approach for metal-based NP activities in a review article was published almost a decade ago to give insight into the *in vivo* behavior and biological effects of nanomaterials, specifically metal-based nanomaterials (MNMs).<sup>23</sup> Robust non-Pt noble metal-based nanomaterials are also well known for their electrocatalytic activity in the hydrogen generation reaction.<sup>25</sup> Noble metal (Au, Ag and Pd) NPs and their composites together with transition metal (Mn, Fe, Co, Ni, Cu, Zn, Cd, Mo and W) nanomaterials and main group metallic (Bi) nanocomposites act as catalysts in CO-selective CO<sub>2</sub> reduction.<sup>27</sup>

Gold-based nanomaterials are highly fascinating for wide research interest in several fields such as catalysis, photonics, sensing of normal cells and bioanalytes due to their stimulating optical properties.<sup>29–33</sup> Gold-based nanomaterials can mainly be grouped into gold-based nanomaterials and bimetallic nanomaterials. The characteristic optical property of gold NPs with a high extinction coefficient is known as surface plasmon resonance (SPR).<sup>34</sup>

Synthetic methods to introduce luminescent properties in gold nanomaterials have been considerably developed within the last one and half years. The photoluminescence (PL)



Table 1 Advantages and disadvantages of organic fluorophores and metal nanoclusters in biological applications

Advantages	Disadvantages
<p>Organic dyes</p> <ul style="list-style-type: none"> <li>• AIE probes are highly luminescent, which is a useful property for bioimaging</li> <li>• Interaction with biomolecules used to trace analyzing the changes in intensity in hydrophilic bioenvironment after aggregation</li> <li>• AIE-organic molecules have resolved the limitation observed in case of conventional organic dyes</li> <li>• AIE organic molecules have longer lifetimes, good quantum efficiency, large stoke shift, enhanced brightness. Efficient energy transfer causes increase in reactive oxygen species generation (ROS)</li> </ul>	<ul style="list-style-type: none"> <li>• Conventional organic dyes showed limited retention time, photobleaching, small Stokes shift, small lifetime (ns), poor quantum yield in NIR region</li> <li>• Pretreatment required to overcome limitation such as photostability for biological application</li> <li>• Lower internalization due to hydrophobic nature, low ROS for PDT and PTT applications, less biocompatibility</li> <li>• Sterically hindered bulky group results in low emissive twisted intramolecular charge transfer (TICT) and low quantum yield.</li> </ul>
<p>Luminescent nanoparticles</p> <ul style="list-style-type: none"> <li>• Enhanced permeability and retention (EPR) effect as compared to organic dyes</li> <li>• Efficient excretion and high biocompatibility</li> <li>• Surface engineering possible for improving cellular interaction and organ distribution</li> <li>• Higher lifetime (<math>\mu</math>s) increase the probability of singlet oxygen species for disease therapy</li> <li>• Photobleaching resistant</li> <li>• NIR based luminescent nanomaterials allows deeper tissue penetration</li> </ul>	<ul style="list-style-type: none"> <li>• Emission can be quenched due to several factors such as pH, buffers, biothiols, metal ions</li> <li>• In order to overcome Luminescence quenching due aggregation, surface functionalisation needed</li> <li>• Rapid renal clearance and short circulation time decrease tumor target efficiency</li> </ul>

properties of gold nanoclusters (AuNCs) have been altered significantly *via* the traceless removal of two kernel atoms through thermal treatment.<sup>35</sup> Rod-shaped icosahedral AuNCs have been reported with bright NIR-II PL from the suppression of non-radiative transitions by the central gold atom in AuNCs to a state with near-zero oscillator strength in the ground-state geometry.<sup>36</sup> In 2021, opposite to the classical concept of the heavy atom effect, the NIR lifetime of photoluminescence from AuNCs has been enhanced in the presence of iodine.<sup>37</sup> Rare earth-doped luminescent microparticles were transformed to an air-stable single crystal with the help of plasmonic gold nanoislands.<sup>38</sup>

T. Pradeep's group reported bright-pink luminescence under UV light by synthesizing AuNCs through the electricity from a triboelectric generator.<sup>39</sup> The same group also prepared luminescent silver-gold nanocomposites by combining silver nanoclusters (AgNCs) and gold nanorods (AuNRs).<sup>40</sup> Pavelka *et al.* combined AuNCs and AuNRs in a compact core-shell nanostructure with a tunable geometry and plasmon-enhanced luminescence properties.<sup>41</sup> Emission enhancement is also possible through a hybrid hydrogel as a cross-linker on AuNCs.<sup>42</sup> Biomolecules, such as enzymes, proteins and polysaccharides, have been explored employing the luminescence from gold nanomaterials.<sup>43–45</sup> In 2020, we explored an assembly of gold nanoparticles (AuNPs) with cucurbit[8]uril to develop a supra-pyramid for drug delivery.<sup>46</sup> Recently, Huang *et al.* used an assembly of AuNCs with cucurbit[n]uril for luminescence switching.<sup>47</sup>

Mechanistic models through experiments<sup>48</sup> and theory<sup>49</sup> have been considered to determine the origin of the visible and NIR luminescence in AuNCs and BMNCs. Recent developments on the luminescent properties of gold nanomaterials involve two-photon excited luminescence,<sup>50,51</sup> light-emitting diodes,<sup>52</sup> prodrug activation,<sup>53</sup> manipulation of surface charge

effect,<sup>54</sup> nanothermometry,<sup>55</sup> molecular recognition,<sup>56</sup> encapsulation<sup>57</sup> and optical fibers.<sup>58</sup>

The most common applications of luminescent gold nanomaterials have been observed in sensing applications by varying their luminescence intensities in the presence of target analytes. Metal ions<sup>59,60</sup> such as  $\text{Cu}^{2+}$ ,  $\text{Hg}^{2+}$ , and  $\text{Fe}^{3+}$ , small molecules<sup>61–67</sup> such as protons,  $\text{CN}^-$ ,  $\text{H}_2\text{O}_2$ ,  $\text{H}_2\text{S}$ , pyrophosphate, dicofol, and ciprofloxacin, and biomolecules<sup>68–70</sup> such as alkaline phosphatase, uric acid, glucose and glucose oxidase are important classes of targets reported since 2021. Another notable detection is the hepatitis B virus through the luminescence properties of AuNCs.<sup>71</sup>

The most challenging application of any luminescence system is the imaging of the probe or material in biological cells and living systems. This challenge has been successfully overcome in cancer cell lines<sup>72,73</sup> such as HeLa and MCF-7 cells, in the tumor imaging of mice<sup>74</sup> and in zebrafish models.<sup>75</sup> Besides sensing and imaging applications of gold nanomaterials due to their SPR peak or luminescence properties, they have several applications including real-time observation of the temperature variation in targeted cancer cells,<sup>76</sup> luminescence resonance energy transfer,<sup>77</sup> screening of synthetic cannabinoids<sup>78</sup> and antibacterial applications.<sup>79,80</sup>

The atomic-level synthetic approach for the preparation of noble metal NPs and the complexity in their synthetic process have been discussed in recent reviews (Table 2).<sup>34,81–93</sup> Simultaneously, the correlation of the atomic-level modification of the surface of nanomaterials with their corresponding catalytic activity is important for understanding the role of metal doping in these NPs. The sensing applications of these metal-incorporated nanomaterials depend on their inherent luminescent property. In the current review, we focus on the mechanistic aspects of the origin of the luminescence in gold-based nanomaterials with a greater emphasis on gold-based nanomaterials and also discuss



Table 2 Recent review articles on synthesis of luminescent gold nanocluster

S. No.	Material	Luminescence properties	Synthesis discussed	Ref.
1.	Metal nanocluster-based hybrid nanomaterials	Ligand-to-metal charge transfer mechanism, FRET, increasing ligand rigidification, AIE, and confinement, Electrochemiluminescence (ECL)	Hybridizing metal nanoclusters with organic molecules, 1D nanomaterials such as nanorods, nanowires, nanotubes and nanofibers, 2D nanostructures such as graphene, metal hydroxides, metal oxides, boron nitride and carbon nitride, 3D nanostructure such as mesoporous silica zeolites, metal-organic frameworks (MOFs), nanogels and mesoporous metal oxides	81
2.	Gold nanoclusters	FRET, PET, disaggregation/aggregation, and change of ligand conformation, AuNCs based sensor advantages such as photostability, large Stokes shift, biocompatibility	Bottom up approach involving such as electrochemical reduction, sono-reduction, photoreduction, chemical reduction using template synthesis and ligand protected AuNCs; top down approach using solvent and ligand induced etching	82
3.	Metal nanoclusters	Enhancement in luminescent properties dependent on composition, structure, oxidation state of metal nanoclusters metal core, structure and steric hindrance of metal nanocluster ligand shell	Synthetic approaches for highly luminescent metal nanoclusters using metal doping, surface motif engineering, ligand engineering, structure modulation of metal nanoclusters	83
4.	Metal nanoclusters	Aggregation induced emission	Brief discussion of synthetic strategies for aggregation induced emission active nanoparticles	84
5.	Alkynyl protected metal nanoclusters	Ligand effect on luminescence property, thermally activated delayed fluorescence, NIR emission	Synthetic method such as comproportionation, anion-templated, solvothermal, post-synthetic ligand exchange method and one pot synthesis; synthesizing alkynyl protected AuNCs <i>via</i> nuclear transformation and reassembly	85
6.	Metal nanoclusters	Luminescence mechanism based on quantum confinement, LMMCT/LMCT, aggregation induced emission, factors affecting luminescence properties such as size and composition of metal core, surface ligand, temperature, pH, and solvent viscosity.	Top down and bottom up synthesis	86
7.	Metal nanoclusters	Absorption and fluorescence properties, two-photon absorption, electrochemiluminescence, solvatochromic effect, polarized emission and fluorescence lifetimes	Top down and bottom up synthesis	87
8.	Chiral gold based nanoassemblies	CD and luminescence based biosensing application	Different biomolecule modulated chiral gold assemblies	88
9.	DNA-template metal nanoclusters	Fluorescence based ion detection, enzyme detection and biomolecule detection, bioimaging	Synthesis of ss-DNA, dsDNA, triplex DNA, quadruplex DNA, higher-order DNA, Vacuum sputtering method for luminescent gold nanoclusters	89
10.	Metal–metal oxide nanoparticles	—	—	90
11.	Noble metal nanostructure–serum albumin interaction	Luminescence dependent on the binding process and plasmonic NPs – serum albumin interactions	—	91
12.	DNA templated silver nanoclusters	Impact of DNA sequence and Ag nanoclusters structure on the optical properties	Synthetic methodologies based on interaction of Ag <sup>+</sup> with homobase DNA strand, helix duplexes <i>via</i> interplanar H-bonds, homobase and heterobase Ag <sup>+</sup> -mediated duplexes	92
13.	Protein protected metal nanoclusters	Fluorescence enhancement strategies, structure dependent optoelectronic properties	One pot synthesis	93

different parameters affecting their luminescence intensity. Also, the role of heterometals on the luminescence intensity of gold-based nanocomposites is illustrated. We attempt to discuss in detail the different synthetic routes for gold-based nanomaterials by classifying them based on their surface capping agents (Scheme 1).

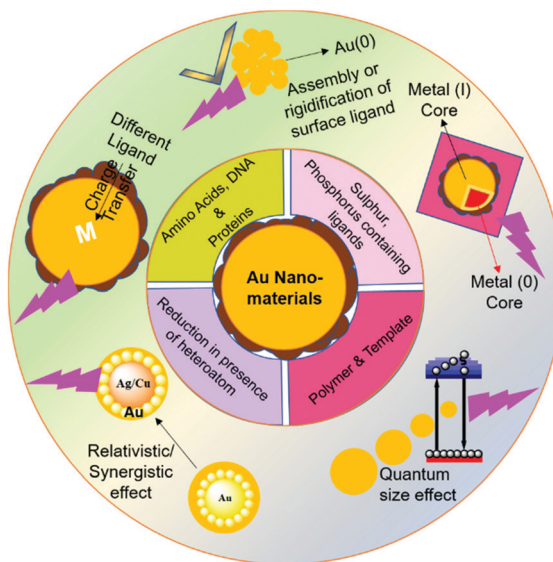
## 2. Origin of luminescence in gold nanomaterials

The synthesis of luminescent nanomaterials and their application in real life are possible by acquiring clear insight into the origin of the luminescence from different nanomaterials at the

molecular and electronic levels. This section of the review discusses the mechanisms behind the origin of the luminescence in gold-based nanomaterials and bimetallic nanoclusters (BMNCs).

Noble metal NPs basically constitute two types of particles based on their size and intrinsic properties. The larger particles ( $\sim$ size  $>$  2 nm) behave as plasmonic nanomaterials possessing the fascinating surface plasmon absorption band, which originates due to the collective oscillation of the surface free electrons, while absorbing the incident light of wavelength, similar to the frequency of oscillation properties.<sup>94,95</sup> Given that these plasmonic NPs possess a larger particle size, their electronic states involve a greater number of gold atoms and result in the disappearance of their molecular bandgap. Due to the





**Scheme 1** Schematic illustration of ligand-based synthesis and origin of luminescence in gold-based nanomaterials.

absence of this band gap, the electron hole recombination process is absent in these NPs, leading to the disappearance of their emission properties.<sup>96</sup>

Alternatively, when the size of the particle decreases ( $\sim$  size  $< 2$  nm), the properties associated with the bulk metal readily disappear. When the size of the particle finally approaches the Fermi wavelength of electrons, the electronic motion gets severely restricted due to the confinement of the electrons. Consequently, the continuous electronic energy band structure transforms into discrete energy states, which are the origin of molecule-like behavior in these ultrasmall NPs. These changes in electronic structure yield fascinating optoelectronic properties such as PL, molecular chirality, redox behavior and intrinsic magnetism.<sup>94,97-99</sup> Due to the quantum confinement effect, the photo-induced excited electrons jump to a higher energy level and get radiatively relaxed in discrete energy levels. This radiative energy appears in the form of light, leading to ultrabright luminescence.

The proposed energy band structure for the origin of the emission in gold NCs was first reported by A. Mooradian, who demonstrated PL in gold NCs by exciting them with a high-energy laser.<sup>100</sup> The direct recombination of electrons and holes *via* interband transitions between the valence band (d band) and conduction band (sp band) is mainly responsible for the origin of their emission properties. It has been fifty years since the first proposed theory on AuNCs, but their legacy continues to date given that several new observations appeared in the emission properties by applying different influencing parameters.

## 2.1 Key and influencing factors for the origin of luminescence in AuNCs

The above-mentioned observations are solely based on the size of AuNCs, which is considered as the key factor for the origin of

their luminescence. The corresponding wavelength for excitation and emission is highly dependent on the size (quantum size effect) of the MNCs. A decrease in size leads to an increase in the relaxation energy gap of electrons, which eventually causes a hypochromic shift in the emission wavelength.<sup>101</sup> However, the emphasis on the optical properties of AuNCs during the last two decades revealed several exceptions in their luminescence properties.

For example, an explanation for the dual emission in  $\text{Au}_{28}(\text{SG})_{16}$  NCs (corrected as  $\text{Au}_{25}$  in later works) could be presented after Link *et al.* proposed their energy band structure by considering the solid-state model and molecular model for the origin of the two luminescence bands in  $\text{Au}_{28}(\text{SG})_{16}$  NCs.<sup>102</sup> It was reported that both the radiative intraband transition (sp-sp) and the radiative interband recombination (sp-d) in the HOMO-LUMO gap contribute to the low and high energy luminescence bands, respectively. Thiolated gold NCs are being extensively studied given that they possess several fascinating size-independent emission properties. For example, with the same core size in  $\text{Au}_{25}$  NCs but different ligands, their emission and excitation spectra are modified.<sup>103,104</sup>

Alternatively, the discovery of aggregation-induced emission (AIE) led to the nanoscale community identifying the major factors that can influence the luminescence properties of nanomaterials.<sup>105</sup> Besides particle size, this review summarizes the major influencing factors that affect their luminescence properties in detail.

**(i) Influence of surface stabilizing ligand.** In  $\text{Au}(\text{I})$ -thiolated MNCs, their luminescence properties can be highly influenced by their surface-stabilizing ligands.<sup>106</sup> Nuzzo and coworkers synthesized different monolayer-protected Au clusters (MPCs). By employing polar or charged ligands in the nonpolar MPC monolayers *via* the ligand exchange method, the emission properties could be induced in the system.<sup>107</sup> Later, the same group correlated the increase in the NIR emission intensity of  $\text{Au}_{38}$  and  $\text{Au}_{140}$  NCs with the increase in the proportion of polar thiolate ligands. The effect of electron-withdrawing ligands and the positive charge on the cluster core resulted in greater polarization in the Au-S bond, hence causing an enhancement in luminescence intensity.<sup>108</sup> Perez-Prieto and coworkers introduced luminescence property in naked NCs by simply passivating thiols and AMP.<sup>109</sup>

Further, Jin and coworkers profoundly studied the effect of ligands on the luminescence properties of  $\text{Au}_{25}$  NCs. The  $\text{Au}_{25}$  NCs were composed of an  $\text{Au}_{13}$  core surrounded by six dimeric  $\text{Au}_2(\text{SR})_3$  staple motifs. It was observed that the luminescence intensity depends on the alkyl chain length and the charge-donating ability of the ligands (Fig. 2A). The charge transfer from the ligands to the metal core *via* S-Au bonds and the electropositive nature of the metal core support the remarkable increase in luminescence intensity (Fig. 2B).<sup>104</sup>

Aiken's group provided theoretical insights into the origin of luminescence in  $\text{Ag}_{25}(\text{SR})_{18}^-$  NCs.<sup>110</sup> They utilized density functional theory (DFT) and time dependent DFT to calculate the geometric and electronic structural changes during the excitation. The emission from  $\text{Au}_{25}(\text{SR})_{18}^-$  nanoclusters involves



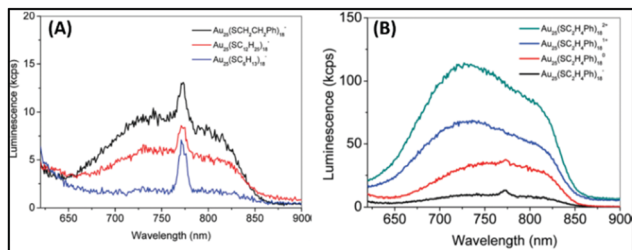


Fig. 2 Emission spectra of (A)  $[\text{Au}_{25}(\text{SR})_{18}]^-$  with R groups (1)  $-\text{C}_2\text{H}_4\text{Ph}$  (black), (2)  $-\text{C}_{12}\text{H}_{25}$  (red), and (3)  $-\text{C}_6\text{H}_{13}$  (blue). (B)  $[\text{Au}_{25}(\text{SC}_2\text{H}_4\text{Ph})_{18}]^q$  ( $q = -1, 0, +1, +2$ ).  $\lambda_{\text{ex}} = 514$  nm. Note: spike at  $\sim 770$  nm in (A) is an artifact from the quartz cell. Reproduced from ref. 104 with permission from the American Chemical Society. Copyright 2010.

several excited states, where the core-based transitions involve superatomic P orbitals and D orbitals. In the lowest energy excited states of  $\text{Au}_{25}(\text{SR})_{18}^-$  nanoclusters, the energy levels of the frontier orbitals are significantly influenced because of the geometric relaxation factors. This phenomenon generates a Stokes shift for  $\text{Au}_{25}(\text{SH})_{18}^-$ , which can exhibit a larger value in the presence of a longer ligand.

Recently, Zhou *et al.* proposed the mechanism behind transient absorption spectroscopy analysis.<sup>111</sup> The  $\text{Au}_{13}$  core of the NCs is mainly associated with UV-vis absorption. The luminescence is observed due to the rapid relaxation of the excited electrons from higher core states to a lower core state and surface state. When excited by UV light (350 nm), the multiexponential decay from the surface state leads to the generation of visible PL (750 nm), whereas the mono exponential decay from the core state results in NIR PL (1100 nm), as shown in Fig. 3. However, lower energy NIR light can only excite the lower core state, preventing the core to surface charge transfer. The visible PL of NCs depends on their surface ligands given that the origin of the PL is associated with core–shell charge transfer. Recent review and reports also shed some light on the ligand-dependent luminescence in AuNCs.<sup>112–114</sup>

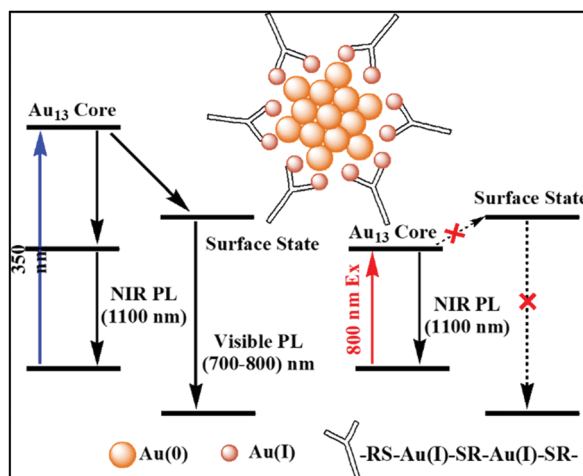


Fig. 3 Schematic diagram of  $\text{Au}(0)$  core and  $\text{Au}(I)$ -thiolate shell  $[\text{Au}_{25}(\text{SR})_{18}]^-$  and the mechanism behind the visible and NIR emissions; adapted from ref. 111.

These interesting observations explain how the surface-stabilizing ligands in MNCs play a significant role in enhancing their luminescence properties *via* LMCT (ligand to metal charge transfer), LMMCT (ligand to metal–metal charge transfer) or LMCCCT (ligand to metal cluster core charge transfer).

(ii) **Influence of self-assembly/aggregation.** Emissive  $\text{Au}(I)$ -thiolate complexes have been known for nearly 15 years.<sup>115</sup> One interesting finding in this field is the aggregation or assembly of NCs, which plays a significant role in the property commonly known as aggregation-induced emission (AIE). Xie and co-workers extensively studied the origin of the emission in the  $\text{Au}(I)$ -thiolate complexes and  $\text{Au}(0)@\text{Au}(I)$ -NCs.<sup>116</sup> The non-emissive aqueous solution of  $\text{Au}(I)$ -thiolate complexes get aggregated by adding either polar solvents or cations, eventually leading to a several-fold increment in luminescence intensity. As the amount of aggregation increases, the  $\text{Au}(I)$  particles get closer, causing the intra- and inter-complex aurophilic  $\text{Au}(I)\cdots\text{Au}(I)$  interactions to become dominant. During the aggregation, these inter- and intra-complex aurophilic interactions significantly restrict the intramolecular vibrations and rotations of the complexes.

Hence, after excitation, the probability of nonradiative relaxation is significantly reduced, which eventually assists in the luminescence enhancement. By selective reduction and controlled aggregation, highly emissive  $\text{Au}(0)@\text{Au}(I)$ -thiolate NCs can be prepared (Fig. 4).

In 2016, the same group prepared a highly luminescent nanogel by utilizing the electrostatic attraction between chitosan and thiolate ligands.<sup>117</sup> This interaction hampered the intramolecular motions of the surface ligands on the Au nanoclusters, which led to an enhancement in luminescence. The AIE origin and the emission energy also depend on the length of the  $\text{Au}(I)$ -SR motif. Recently, Heyon and coworkers synthesized a luminescent gold cluster assembly using mercapto-carboxylic acid and  $\text{Zn}^{2+}$  ions as the coordinating metal.<sup>118</sup> The rigidification of the ligands through coordination with  $\text{Zn}^{2+}$  and the aurophilic interaction among the  $\text{Au}_4$  clusters were mainly responsible for the bright greenish-blue fluorescence. Recently, several reports have demonstrated the AIE effect in AuNPs, which were utilized as fluorescent sensors and in bioimaging.<sup>119–125</sup> Recent reviews on the aggregation and self-assembly of nanoclusters shed light on the nanoscale forces/interactions such as dipolar attraction, van der Waals interactions, electrostatic interactions,  $\pi$ – $\pi$  stacking, and metallophilic interactions, which can initiate the aggregation or assembly process in nanoclusters.<sup>11,126,127</sup>

(iii) **Influence of oxidation state of Au.** Recent studies on gold-based nanoparticles suggested that the presence of a fraction of  $\text{Au}(I)$  generates intrinsic luminescence in NPs. Zheng and co-workers were the first to report this discovery, while varying the  $\text{GSH}:\text{Au}$  ratio to synthesize glutathione-stabilized AuNPs.<sup>128</sup> The synthetic process resulted in two different NPs with orange and yellow emission and their lifetime changed from micro- to nanoseconds when the excitation wavelength changed from 420 to 530 nm, as shown in Fig. 5. The XPS spectra of these NPs indicated the presence of a significant

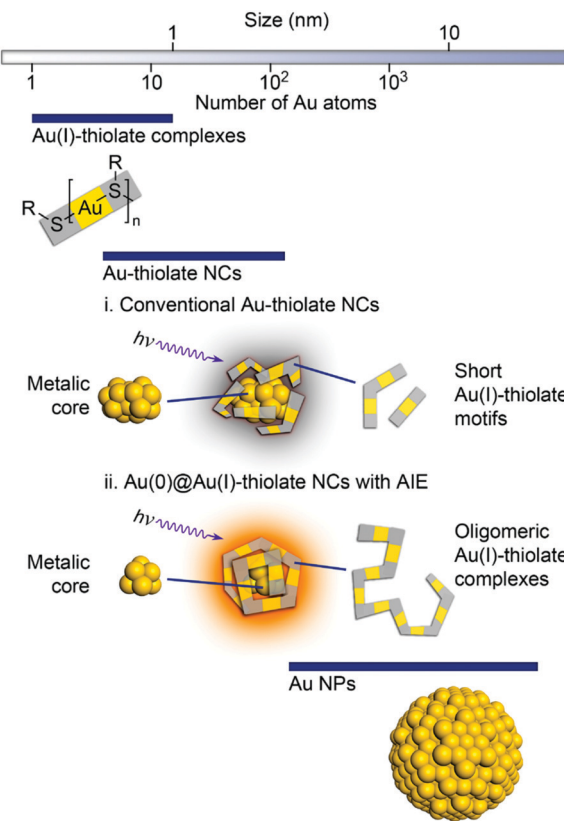


Fig. 4 Schematic illustration of the structures of (i) conventional Au-thiolate NCs with short Au(I)-thiolate motifs and (ii) luminescent Au NCs with AIE. Reproduced from ref. 116 with permission from the American Chemical Society, Copyright 2010.

amount of Au(I). A strong reducing agent induced quenching of the emission, demonstrating the important role of the oxidation state of Au towards PL. The authors hypothesized that the generation of luminescence is due to the LUMO (sp band) to HOMO (d band) transitions. The microsecond emission lifetime originated from the triplet excited states in the sp band, where gold was mixed with the p orbitals of sulfur. When excited near 530 nm, the nanosecond lifetime suggested the resultant emission was correlated with the transition between singlet excited states and ground states. The degeneracy in the singlet and triplet excited states was responsible for the different lifetimes under different excitation wavelengths. Similar observations have also been reported in other reports.<sup>129,130</sup> Tang and co-workers demonstrated that the small energy gap between the singlet and triplet excited states resulted in long luminescence decay components in Au<sub>25</sub> NCs.<sup>131</sup> Recently, we also reported the role Au(I)/methionine metallic bonds.<sup>132</sup> Another interesting observation, which deals with the interaction towards the generation of emissive properties in nucleated Au(0)/Au(I) NPs in aqueous medium, was reported.<sup>132</sup> The interaction of methionine with Au(I) led to the inhibition of secondary nucleation during the growth reaction of AuNPs. At a lower concentration of Au salt, this inhibition resulted in the generation of luminescent NPs (2.8 nm). The emission properties were

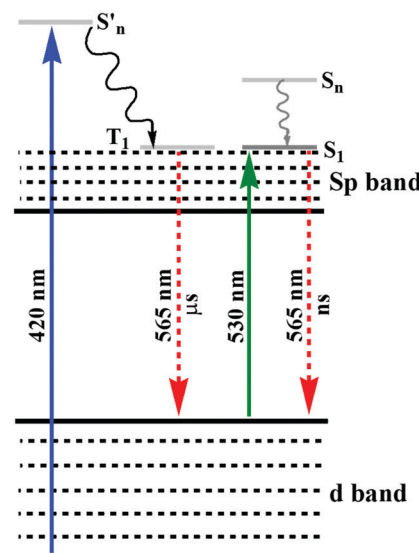


Fig. 5 Luminescence involving d and sp bands of orange-emitting GS-AuNPs.

quenched during the growth reaction with a high concentration of Au salt, which led to the generation of larger nucleated particles. Other than AIE properties,<sup>133,134</sup> interesting observations were reported for bimetallic NCs, where either of the monometallic NCs emitted weakly under illumination.

However, a remarkable enhancement in the luminescence intensity of several folds was obtained from their corresponding bimetallic counterparts after controlled doping of a particular metal. For example, Jin and co-workers reported the significant enhancement of the quantum yield (QY) of weakly emissive Au<sub>25</sub> nanorods (Au<sub>25</sub>(PPh<sub>3</sub>)<sub>10</sub>(SC<sub>2</sub>H<sub>4</sub>Ph)<sub>5</sub>Cl<sub>2</sub><sup>+</sup>) from 0.1% to 40.1% by simply replacing 13 Au atoms methodically by Ag atoms (Ag<sub>13</sub>Au<sub>12</sub>, species II) in the metal kernel without affecting their structural architecture (Fig. 6a–c).<sup>135</sup>

The authors also experimentally demonstrated that the doping of 12 silver atoms (Ag<sub>12</sub>Au<sub>13</sub>, species I) in the parent NC did not result in similar absorption and emission properties even after maintaining an analogous ligand environment. They successfully correlated the HOMO–LUMO energy gap with different experimental techniques. It has been reported that the 6s and 6p atomic orbitals of the ten Au waist atoms (Fig. 6c) are deeply associated with the HOMO in Au<sub>25</sub> NC (Fig. 6d), whereas the LUMO is mainly contributed by the central Au atom.<sup>136,137</sup> The 13th doping with silver atoms in the parent NC involves the replacement of the central Au atom by an Ag atom, and hence the large perturbation of electronic states remarkably influenced the LUMO→HOMO transition. This is mainly due to the relativistic effect in gold involving the dominant *sd* hybridization. After doping with 13 Ag atoms, the LUMO energy shifted due to the involvement of the 5s orbital of Ag and the LUMO→HOMO band gap increased, and hence the recombination of excited electrons involves highly intense emission. A comparatively similar observation was also reported experimentally for Ag<sub>29</sub>(BDT)<sub>12</sub>(TPP)<sub>4</sub> NC (BDT: 1,3-benzenedithiol)



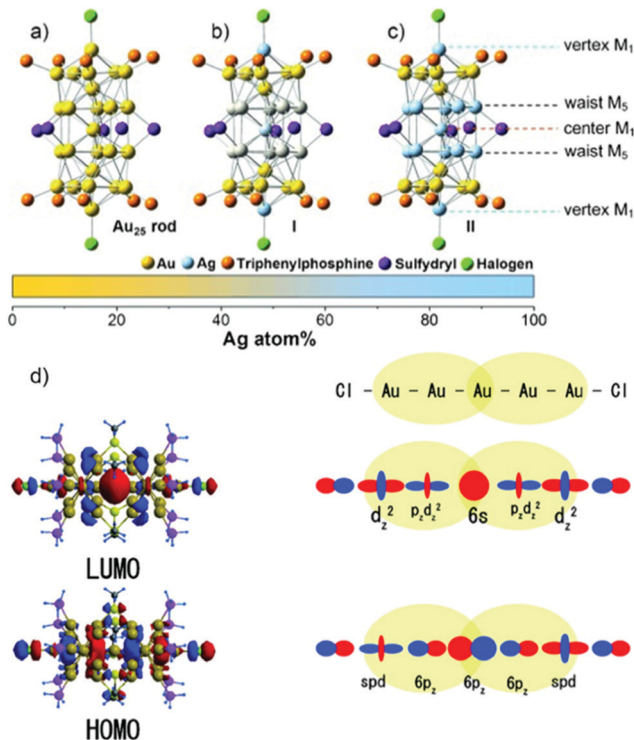


Fig. 6 Crystal structures of (a)  $\text{Au}_{25}$  NCs and (b) and (c)  $\text{Ag},\text{Au}_{25-x}$  with a probability of (I) 12 and (II) 13 doping Ag atoms, M = metal atom. (d) HOMO and LUMO of species II together with metal orbital participation for absorbance. Spheres with color green, red, yellow, pink and grey represent Ag, Au, S and C, respectively. H atoms are omitted for simplicity. (a)–(c) reproduced with permission.<sup>135</sup> Copyright 2014. Wiley-VCH. (d) Reproduced from ref. 136 with permission from the American Chemical Society. Copyright 2007.

and TPP: triphenylphosphine), where gold doping was the origin of the anomalous behavior in the absorption and luminescence signal in  $\text{Ag}_{29-x}\text{Au}_x(\text{BDT})_{12}(\text{TPP})_4$  by applying density electronic relaxation, and the electronic modulation in  $\text{Ag}_{29-x}\text{Au}_x(\text{BDT})_{12}(\text{TPP})_4$  ( $x = 1\text{--}5$ ) induced a similar enhancement in luminescence and structural stability.<sup>138</sup> This is mainly possible due to the doping-induced perturbation in the structures.<sup>138</sup>

By considering the importance of the relativistic effect, Dolg and co-workers also theoretically established density functional theory (DFT) and time-dependent density functional theory (TD-DFT) approaches towards the geometric and electronic structures.<sup>139</sup> The replacement of Ag by Au atoms significantly alters the recombination path of excited electrons through effective orbital contributions. After considering the relativistic effect, the theoretical calculations also indicated that the controlled increase in the Au doping inside the  $\text{Ag}_{29-x}\text{Au}_x(\text{BDT})_{12}(\text{TPP})_4$  NCs remarkably lowered the centroid of charge of the excited electrons and holes. These phenomena overall enhanced the luminescence intensities of  $\text{Ag}_{29-x}\text{Au}_x(\text{BDT})_{12}(\text{TPP})_4$  NCs ( $x = 3\text{--}5$ ). It was also reported that the sensitization of QY and PL enhancement factor are highly dependent on the number of possible hetero annular  $d^{10}\text{--}d^{10}$  metallic bonds.<sup>140</sup> Another interesting observation, which deals with the synergistic

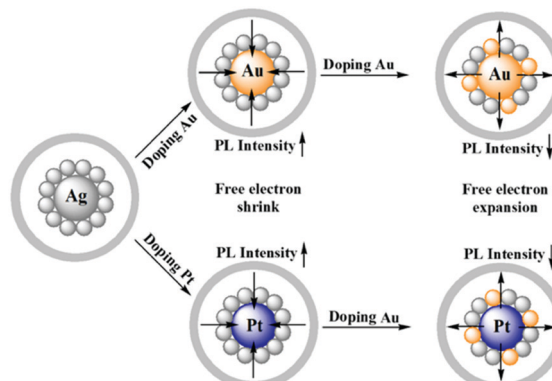


Fig. 7 Schematic illustration of the shrinkage and expansion of free electrons due to Au doping.

effect originating from the presence of two different  $d^{10}$  metals in the close proximity, has been reported for cooperatively sensitizing their luminescence and altering their basic properties such as stability and catalytic activity.<sup>138,141</sup> During the last decade, several reports have been reported on this co-operative luminescence enhancement effect in the case of bimetallic NCs. The synergist effect of silver particularly plays an important role through the doping of Ag in AuNCs.<sup>142–144</sup>

Zhu and co-workers experimentally demonstrated the anomalous blue-shifting followed by broadening in the absorption spectra and enhancement in PL intensity with limited Au and Pt doping in  $\text{Ag}_{25}(\text{SPhMe}_2)_{18}\text{PPh}_4$  NCs.<sup>145</sup> The PL intensity enhanced during the replacement of the central Ag atom of the icosahedral Ag core by an Au or Pt atom. However, further Ag atom substitution exceptionally quenched the PL intensity.

The origin of the selective PL intensity enhancement can be attributed to the high electron affinity of Au or Pt atoms. These metal atoms contribute more towards the super atomic orbitals of the NCs and force the free valence electrons to shrink towards the central atom (Fig. 7). In contrast, more substitutions on the periphery of the icosahedral core result in a significant change in the electron density inside the  $\text{M}_{13}$  core, which expands the core size, leading to the emission quenching process. Recently, Antoine and coworkers demonstrated the controlled doping of silver atoms in  $\text{Au}_{10}\text{SG}_{10}$  catenane NCs, which yielded silver-doped  $\text{Au}_{10-x}\text{Ag}_x\text{SG}_{10}$  NCs with different extents of doping (e.g.,  $x = 0\text{--}2$  and  $x = 1\text{--}4$ ).  $\text{Au}_{10-x}\text{Ag}_x\text{SG}_{10}$  with  $x = 1\text{--}4$  showed a blue shift in absorption and a significant red shift in the two-photon emission spectrum in contrast to  $\text{Au}_{10}\text{SG}_{10}$ . In the case of  $\text{Au}_{10-x}\text{Ag}_x\text{SG}_{10}$  ( $x = 1\text{--}4$ ), the improved relaxation of the first excited state ( $\text{S}_1$ ) of silver-doped AuNCs may be the prime reason behind the shifting of the two-photon excited fluorescence (TPEF) towards a longer wavelength.<sup>146</sup>

### 3. Synthetic methods for luminescent gold nanomaterials

In the 21st century, the scientific attention has been shifted partially from the conventional organic fluorophores towards



alternative novel fluorescent metal NCs to fabricate different fluorogenic systems. Several advantages such as excellent stability, good biocompatibility, and high luminescence intensity collectively make metal NCs competitive fluorescent probes aimed at possible applications in different fields.<sup>147–151</sup> Compared to metal NCs comprised of a single metal, BMNCs comprised of heterometals in their system possess better cooperative electronic, optical, sensing and biological properties.<sup>102,138,152–155</sup> This section discusses the synthetic procedures available to synthesize metal-based luminescent nanomaterials.

### 3.1 Gold nanoclusters (AuNCs)

Gold nanoclusters exhibit unique photoluminescence properties, biocompatibility and high renal clearance. Recently, synthetic approaches for water-soluble AuNCs have been explored for various biological applications such as biosensing of metal ions, small molecules, protein and DNA sensors, cell environment sensors and biological imaging.<sup>148</sup> Developing synthetic methodologies can be useful for overcoming the shortcoming observed for the practical applications of AuNCs. The review by Khan *et al.* highlighted the evolution of AuNCs and highlighted the importance of modifying synthetic methods for various biological applications in detail.<sup>84</sup> Surface functionalization is crucial for catalysis given that it protects nanoclusters from aggregation, improves their stability and alters their electronic structure. Recent progress in the surface-modified gold nanoclusters such as thiolate-protected AuNCs, phosphine-protected AuNCs, alkynyl-protected AuNCs and their role in the catalysis and selectivity for oxidation, reduction, cycloisomerization, hydrolysis, heterocoupling and electrocatalysis reactions has been summarized in the review article by Li *et al.* The steric hindrance of ligands, Au active sites, and lattice oxygen atoms are a few factors affecting their catalytic activity.<sup>156</sup> The ongoing research has found that the kernel structure and atomic packing leading to various crystallographic structures, *i.e.*, fcc, decahedral kernels, or NCs with icosahedral kernels, can tune the optical properties and energy gap. Synthetic strategies can be used to control the crystal structure of AuNCs, and hence their electronic and absorption properties.<sup>157</sup>

**3.1.1 Protein and DNA-stabilized AuNCs.** Surface ligands exhibit an important influence on the electronic properties of nanomaterials. The photoluminescence enhancement can be achieved by increasing the number of electron-withdrawing groups on ligands, increasing the positive charge on the Au core, LMCT (ligand to metal charge transfer) or LMMCT (ligand to metal–metal charge transfer), enhanced  $\text{Au} \cdot \cdot \text{Au}$  aurophilic interactions due to aggregation and rigidification.<sup>158</sup> Biomineralization simply involves the interaction and sequestration of inorganic ions. BSA-AuNCs are stabilized by Au–S bonds as a result of the cys residues in BSA and steric hindrance due to bulky ligands.

Xie *et al.* developed a synthetic approach, where BSA sequesters and reduces the  $\text{Au}^{3+}$  ions, forming BSA– $\text{Au}_{25}$  NC bioconjugates with red fluorescence.<sup>159</sup> Their synthesis depends on NaOH, reaction temperature and ratio of BSA and Au concentration. The post-synthesis modification of BSA-stabilized

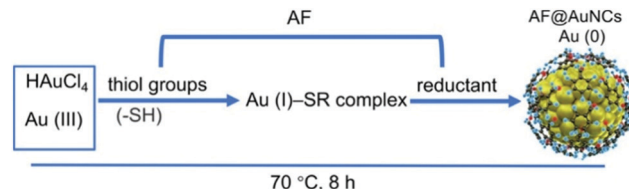


Fig. 8 Schematic illustration of the synthesis of anti-Flt1 peptide (CGNQWFI, AF)-stabilized AuNCs. Reproduced from ref. 161 with permission from the American Chemical Society, Copyright 2021.

AuNCs can be used for enhancing their photoluminescence property by rigidification and increasing their aurophilic interaction. Wong *et al.* modified the methodology utilizing a thermomixer for mixing BSA and  $\text{HAuCl}_4$  solution, which is more advantageous compared to the earlier reported methods because of its short reaction time, higher quantum yield and mild conditions.<sup>160</sup> AuNCs were also synthesized using ligands besides the traditional ligands such as anti-Flt1 peptide (CGNQWFI, AF), as shown in Fig. 8. Li *et al.* reported the one-pot synthesis of AF@AuNCs, where the template plays an important role both as a stabilizer and reductant because of the presence of amino acids such as tyrosine and cysteine.

This template-based synthetic methodology is unique compared to earlier reported methods given that it does not require additional reducing agents.<sup>161</sup> Jain *et al.* reported the synthesis of BSA-coated AuNCs with bright red fluorescence in the dark overnight. The gold nanoclusters synthesized using this method showed a good quantum yield and brightness. The cysteine residues present in BSA stabilized  $\text{Au}^{3+}$  and reduced under alkaline pH.<sup>162</sup> A scheme for the synthesis of BSA-stabilized AuNCs is shown in Fig. 9.

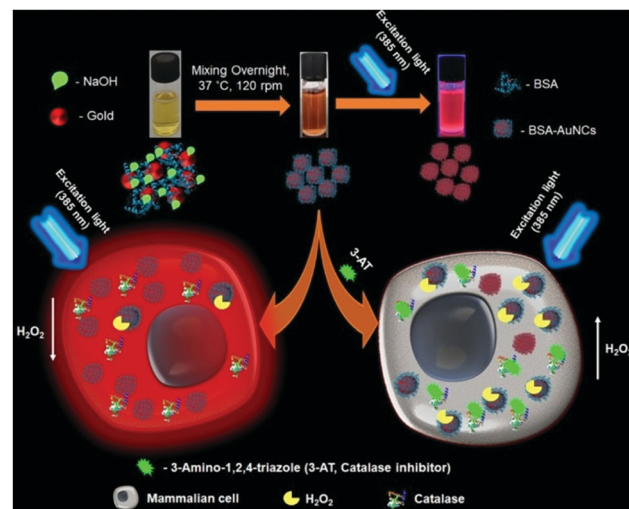


Fig. 9 Schematic illustration of the synthesis of red fluorescent BSA-stabilized AuNCs and changes in the fluorescence intensity in the presence of hydrogen peroxide after treating cells with 3-amino-1,2,4-triazole (catalase inhibitor). Reproduced with permission from ref. 162, Copyright Elsevier (2021).



Hada *et al.* reported the preparation of BSA-stabilized AuNCs, which showed temperature-dependent (in the range of 25 °C to 70 °C) and excitation-induced tunable red PL. The shift in the photoluminescence wavelength with different excitation is considered to be due to the temperature-activated delayed fluorescence (TADF) emission. The temperature-induced conformational changes in BSA led to a decrease in the emission intensity and the change was found to be irreversible in the temperature range of 52–60 °C.<sup>148,163</sup> The gold nanoclusters synthesized using this method exhibited stable reversible photoluminescence with temperature.<sup>164</sup>

Ungor *et al.* reported lysozyme (LYZ), HSA, BSA and gamma globulin ( $\gamma$ G) protein-stabilized AuNCs using the template-assisted method. The AuNCs showed a large lifetime in the microsecond range and average QY% values in the range of 3.8–5.4%.<sup>165</sup> Li *et al.* reported BSA-stabilized AuNCs embedded in self-assembled *N*-fluorenylmethoxycarbonyl diphenylalanine (Fmoc-FF) together with horseradish peroxidase (HRP).<sup>166</sup> Although AuNCs in general do not show pH-dependent fluorescent property, the Fmoc-FF/AuNCs/HRP film showed pH dependency in the pH range of 9.0 to 5.0 due to the structural changes in Fmoc-FF.

Niu *et al.* reported the preparation of BSA-stabilized AuNCs by mixing aqueous  $\text{HAuCl}_4$  solution and BSA solution in the presence of NaOH.<sup>167</sup> The changes in fluorescence intensity were monitored using Cys and  $\text{Cu}^{2+}$ . The fluorescence was enhanced when Cys was added to the AuNCs by filling the surface defects and fluorescence quenching occurred due to the aggregation in the presence of  $\text{Cu}^{2+}$ . The changes in fluorescence spectra with the addition of metal ions such as  $\text{Cu}^{2+}$  and cysteine are illustrated in Fig. 10. Although there are several reports on the protein-templated synthesis of gold nanoclusters, Chakraborty *et al.* reported the preparation of HSA-stabilized  $\text{Au}_{25}$ NCs<sup>168</sup> with a high quantum yield and exceptionally stable photoluminescence property for over a year. AuNCs was encapsulated compactly within the bulky HSA structure *via* reduction by the tyrosine group at a pH greater

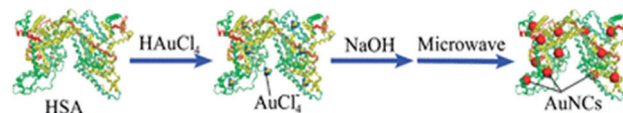


Fig. 11 Scheme for the microwave-assisted synthesis of gold nanoclusters. Reproduced from ref. 169 with permission from The Royal Society of Chemistry, Copyright 2012.

than the  $\text{pK}_a$  of tyrosine with red emission. The nanoclusters exhibited no change in PL property in the range pH range of 3–12 and were highly thermally stable, with a long lifetime ( $>100$  ns) as a result of their triplet–singlet intra-band transitions. Temperature-dependent PL spectra changes were observed due to the conformational changes in the protein structure, as in the case of earlier reported methods for BSA-stabilized AuNCs.

Yan *et al.* reported the microwave-assisted synthesis of BSA-stabilized AuNCs with red emission. HSA-protected AuNCs were synthesized using a similar methodology, as shown in Fig. 11.<sup>169</sup> This methodology is significant for reducing the reaction time but has certain limitations given that the reaction time needs to be strictly monitored considering that continuous MW irradiation leads to the formation of larger NPs with no fluorescence. Protamine-AuNCs with strong fluorescence were synthesized *via* a one-step process.<sup>170</sup> This methodology required mild conditions for the synthesis of protamine-stabilized AuNCs, which can be used for gene delivery and provide a scope for the utilization of AuNCs in the field of biological applications. Zhang *et al.* reported the preparation of cytidine (also known as ribofuranose where cytosine is attached to a ribose sugar)-stabilized green fluorescent AuNCs, as shown in Fig. 12.<sup>171</sup> This green emission is attributed to the intraband transitions of the free electrons in AuNCs. The emission property was found to be red-shifted from 490 to 560 nm and enhanced significantly in the presence of  $\text{AgNO}_3$  due to the Au-Ag metallic bonds. Similarly, the fluorescence was quenched in the presence of  $\text{Hg}^{2+}$  due to the high-affinity metallophilic  $\text{Hg}^{2+}$ - $\text{Ag}^+$  interaction. The enhancement in the emission due to metal doping is expected according to literature reports because of the changes in the nature of the electronic state and orbitals.<sup>158</sup>

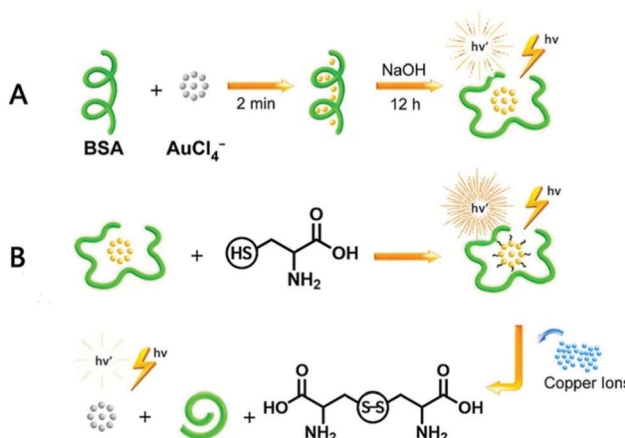


Fig. 10 Schematic illustration of the synthesis of BSA-stabilized AuNCs and effect of  $\text{Cu}^{2+}$  ions and cysteine on their fluorescent property. Reproduced with permission from ref. 167, Copyright Elsevier (2021).

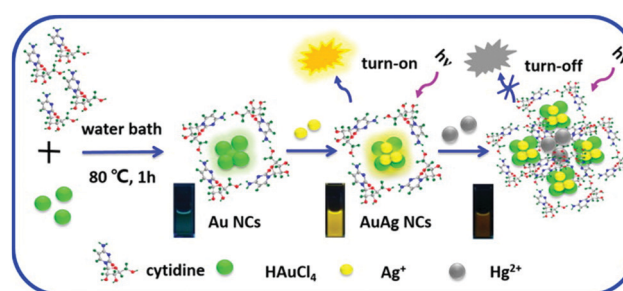


Fig. 12 Schematic illustration of the synthesis of cytidine-stabilized AuNCs and changes in the luminescence property with the addition of  $\text{Ag}^+$  and  $\text{Hg}^{2+}$ . Reproduced with permission from ref. 171, Copyright Elsevier (2015).



Egg shell membrane (ESM) is composed of water-insoluble glycoproteins such as collagen and amino acids such as glycine alanine and uranic acid. Devi *et al.* reported the preparation of Au-ESM-NCs, where ESM acts as a template and interacts with  $\text{Au}^{3+}$ , resulting in change in a color from deep yellow solution to colorless, and the subsequent appearance of a pink/blue color was observed with a broad peak in the visible range (500–750 nm), indicating the reduction to  $\text{Au}(0)$ .<sup>172</sup> This method led to the formation of both  $\text{Au}_8$  and  $\text{Au}_{25}$  clusters. Both broad UV-visible spectra and excitation-dependent emission spectra confirmed the formation of AuNCs of variable size. Blue and red emissive AuNCs were obtained due to the electronic transitions between the sp band and d band and electron-hole recombination. The prepared AuNCs were found to be stable for only up to 15–20 days.

**3.1.1.1 Amino acid-stabilized AuNCs.**  $\text{Au}_{25}(\text{Cys})_{18}$  NCs were synthesized *via* a simple one-pot method in the presence of L-Cys as a stabilizing agent. This methodology enabled the size-controlled synthesis of  $\text{Au}_{25}(\text{SR})_{18}$  NCs on a large scale using CO as a reducing agent.<sup>173</sup> Different stages of the growth and formation of  $\text{Au}_{10-15}$  NCs (20 min),  $\text{Au}_{10-15}$  to  $\text{Au}_{16-25}$  NCs (20–90 min), and  $\text{Au}_{16-25}$  to  $\text{Au}_{25}$  NCs were finally illustrated using UV-Visible spectroscopy and MALDI-TOF analysis.

Gran *et al.* reported the synthesis of  $\text{Au}_{25}(\text{AcCys})_{18}$  using gold salts with acylated Cys in methanol in the presence of different bases.<sup>174</sup> Yang *et al.* reported the synthesis of 6-aza-2-thiothymine (ATT)-protected AuNCs and Arg/ATT-AuNC in the presence of NaOH, involving two steps, as shown in the Table 3. An enhancement in luminescence observed with Arg/ATT-AuNCs as rigid host-guest assemblies formed *via* reduced non-radiative relaxation.<sup>175</sup>

**3.1.1.2 Thiol-stabilized AuNCs.** There are several reports in the literature on the synthesis of GSH-stabilized AuNCs. Liu *et al.* reported the synthesis of GSH-stabilized AuNCs as  $\text{Au}_{25}(\text{SG})_{18}$  with emission in the NIR region ranging from 1100–1350 nm in a reaction vessel saturated with CO at room temperature. The contribution of ligand stabilization (Fig. 13b and c) and metal doping (Fig. 13a, d and e) for enhancing the fluorescence in the NIR II region for  $\text{Au}_{25}$  nanoclusters with a HOMO-LUMO band gap (1.18 eV) was studied in detail. NIR fluorescence images were observed for Cu- and Zn-doped AuNCs (Fig. 13f). The different electronic states for the Au atom and ligand contributing to the HOMO-LUMO energy levels are shown in Fig. 13(g), (h) and (i). The maximum NIR II intensity was found in the case of cysteine. The changes in LUMO energy levels due to S 3p and S 3s electronic states using different surface ligands modulate the fluorescence intensity. Metal doping resulted in a decrease in the band gap to 1.11 eV and 1.08 eV for Cu and Zn, respectively, and the LUMO split into sub-energy levels.<sup>176</sup> Pan *et al.* reported GSH-stabilized AuNCs *via* the reaction of gold chloride salt and GSH at 70 °C under gentle stirring for 24 h.<sup>177</sup>

Gran *et al.* synthesized  $\text{Au}_{10}\text{SG}_{10}$ ,  $\text{Au}_{15}\text{SG}_{13}$ ,  $\text{Au}_{18}\text{SG}_{14}$ ,  $\text{Au}_{25}\text{SG}_{18}$ ,  $\text{Au}_{15}\text{PEG}$  and  $\text{Au}_{25}\text{PEG}$  (PEG represents polyethylene

glycol) using the earlier reported methods.<sup>174</sup>  $\text{Au}_{10}(\text{SG})_{10}$  was prepared at ambient temperature by mixing aqueous gold chloride solution in a methanolic mixture containing GSH and trimethylamine. NaOH solution was added to the reaction solution, and then centrifuged. Centrifugation was done repeatedly by dissolving the resulting product in aqueous  $\text{NH}_4\text{OH}$ , and then again precipitating in methanol. The resultant powder was dissolved in water followed by glacial acetic acid and left undisturbed for 1 h.<sup>178</sup>  $\text{Au}_{15}(\text{SG})_{13}$  was synthesized using the same procedure with slight modification at –10 °C and tetrabutylammonium borohydride ( $\text{TBA-BH}_4$ ) as a reducing agent.<sup>179</sup>

$\text{Au}_{18}(\text{SG})_{14}$  was synthesized by dissolving GSH in methanol, tributylamine and water followed by gold solution and diethyl ether. The NCs were purified initially by dissolving in basic solution, precipitated in MeOH, and further through centrifugation. Tetrabutylammonium borohydride and tetramethylammonium borohydride were added in two parts under strong agitation and stirring in an ice bath. The synthesized nanoclusters after purification were modified to form TBA- and TOA-Au NCs using tetrabutylammonium hydroxide and tetraoctylammonium bromide, respectively. The addition of bulky counterions has been reported to enhance the fluorescence, as shown in Fig. 14, and the solvent-dependent changes in the two-photon excited fluorescence spectra are illustrated in Fig. 15.<sup>180</sup>

$\text{Au}_{25}(\text{SG})_{18}$  was synthesized similarly by stirring gold salt and GSH (1 : 4) in a methanolic solution, followed by the addition of  $\text{NaBH}_4$  as a reducing agent, resulting in a dark-brown precipitate.<sup>103</sup> Huang *et al.* reported GSH-capped AuNCs using a similar procedure.<sup>181</sup> Venkatesh *et al.* reported the preparation of green fluorescent 8-mercapto-9-propyladenine-stabilized AuNCs.<sup>182</sup> During the synthesis, a white precipitate was obtained with the formation of an  $\text{Au}(\text{i})$ -thiolate complex, which was further reduced to AuNCs in the presence of  $\text{NaBH}_4$ .

$\text{Au@MUA}$  NCs were synthesized *via* the method reported by Huang *et al.*<sup>183</sup> Tetrakis(hydroxymethyl)-phosphonium chloride (THPC) in alkaline solution was added as a reducing agent to gold salt followed by MUA stock solution and sodium tetraborate. The reaction mixture was kept in the dark at room temperature for about 72 h and purified by a centrifugal filter and resuspended in sodium borate buffer of pH 9.  $\text{Au@MUA}$  NCs were further stabilized by mixing with ligand stock solution from the same *n*-alkanethiolate family with different carbon chain lengths. Sun *et al.* reported a one-pot approach using water-soluble MUA-stabilized AuNCs.<sup>184</sup> In this synthetic approach, MUA was added to an aqueous solution of gold salt in the presence of NaOH at room temperature, where MUA acts as both a capping and reducing agent.

**3.1.1.3 Polymer-stabilized AuNCs.** Aldeek *et al.* reported the preparation of bidentate LA-functionalized AuNCs with fluorescence in the red to near-infrared region with an emission centered at ~750 nm.<sup>185</sup> LA was first modified with PEG short chain LA-PEG<sub>750</sub>-OCH<sub>3</sub>, LA-PEG<sub>550</sub>-OCH<sub>3</sub>, LA-PEG<sub>600</sub>-COOH, LA-PEG<sub>600</sub>-NH<sub>2</sub> and LA-PEG<sub>600</sub>-N<sub>3</sub> (PEG molecular weights are 750, 550, and 600) or a zwitterion group followed by the



Table 3 Synthesis of gold nanolusters

Reagent added	Surface capping agent	Reaction condition	$\lambda_{\text{ex}}$ (nm)	$\lambda_{\text{em}}$ (nm)	size(nm)	QY%	Brightness ( $\text{M}^{-1} \text{cm}^{-1}$ )	Ref.
NaOH (pH 12)	BSA	37 °C, 12 h	480	640	0.8	6%	$1.26 \times 10^3$	159
NaOH	BSA	60 °C, 6 h	365	630	<2.0	10.62%	$3.80 \times 10^6$	160
—	Anti-Flt1(AF) peptide	70 °C, 8 h	328	620	1.9	9.92%	$5.39 \times 10^6$	161
NaOH	BSA	37 °C, dark, overnight	511	651	3.18	95.84%	$1.26 \times 10^6$	162
Ascorbic acid NaOH	BSA	37 °C, 36 h	530	670	2-3	NA	—	164
NaOH (pH 12)	Lysozyme	40 °C, 24 h	350	645	1.3	3.8%	—	165
NaOH	HSA	40 °C, 24 h	350	650	1.4	4.1%	—	165
—	yG protein	40 °C, 24 h	40	645	1.5	4.4%	—	165
NaOH	BSA	40 °C, 24 h	40	660	1.4	5.4%	—	166
Fmoc-FF, HRP, BSA-AuNCS	BSA	37 °C, 12 h	500	660	3.7	—	—	166
NaOH	BSA	4 °C, 12 h	365	660	—	—	—	166
NaOH	HSA	37 °C, 12 h	495	660	3.0	—	—	167
NaOH	HSA	40 °C, 18 h	505	660	1.7	12%	$1.20 \times 10^5$	168
NaOH	BSA	MW radiation (300 W)	645	510	5	—	—	169
NaOH	HSA	6 min	640	514	—	—	—	170
NaOH	Proline	37 °C, 12 h	280	600	1.65	—	—	171
NaOH	Cytidine	80 °C, 1 h	370	490	1.50	—	—	171
NaOH (pH 11)	Egg shell membrane	RT	335	440	<20	—	—	172
NaOH (pH 11)	Cysteine	Sealed reaction vessel, CO, RT, 24 h RT	585	630	—	—	—	173
—	N-Acetyl-L-cysteine(methanol)	RT	—	—	—	—	—	174
Tributylamine, triethylamine, $\text{NH}_4\text{OH}$	6-Aza-2-thiothymine (ATr)	Dark, 1 h, RT	423	532	3.0	0.03%	$1.10 \times 10^3$	175
NaOH (pH 8.0)	37 °C, 24 h	423	532	3.0	67.02%	$2.49 \times 10^4$	175	
ATT—AuNcs (pH 11)	CO, RT, 24 h	808	1120	<2.0	0.05%	$6.55 \times 10^2$	176	
NaOH (pH 11)	70 °C, 24 h	365	580	2.5	—	$1.65 \times 10^3$	177	
—	Ag <sup>+</sup> glutathione	RT, overnight	420	510	—	$1.2 \times 10^3$	$1.32 \times 10^4$	178
NaOH, $\text{NH}_4\text{OH}$ , Methanol, glacial acetic acid	Glutathione (methanol & triethylamine)	Mixed at -10 °C, 1 h and stirred overnight at RT	435	820	—	$3 \times 10^{-3}$	$3.6 \times 10^3$	179
Tetrabutylammonium borohydride	Glutathione (methanol & triethylamine)	Ice bath 3 h	Two-photon excited at 780	600	—	—	—	180
Tetrabutylammonium borohydride, tetramethylammonium borohydride	Glutathione (methanol)	0 °C, 1.5 h	514.5	700	0.7	—	8.8	103
—	Ag <sup>+</sup> glutathione	90 °C, 6.5 h	370	615	1.71	$0.22\% \text{ (pH 7)}$	$2.60 \times 10^2$	181
NaBH <sub>4</sub>	8-Mercapto-9-propyladenine	MeOH·H <sub>2</sub> O (1:1)	365	510	2	$0.15\% \text{ (pH 11)}$	$1.80 \times 10^2$	182
—	THPC (alkaline solution), 11-mercaptopentadecanoic acid	Dark, RT, 72 h	675	520	$1.2 \times 10^{-2}$	$5.58 \times 10^4$	183	183
NaOH	11-Mercaptopentadecanoic acid	RT, 5 h	285	608	1.8	2.4%	$2.14 \times 10^4$	184
NaOH, NaBH <sub>4</sub>	PhC <sub>6</sub> H <sub>4</sub> SH (added two times)	RT, 15 h	365	750	1.2	14%	$8.8 \times 10^4$	185
TOAB & HauCl <sub>4</sub> (THF), NaBH <sub>4</sub>	Ultrasound, evaporation	total reaction time 28 h	400	650	$1.32 \pm 0.66$	—	—	186
BM-Au Ncs (THF), water	DSPE-PEG <sub>5000</sub> (THF)	Ultrasound, evaporation done reduced pressure at 40 °C	400	650	$62 \pm 18$	—	—	186



Table 3 (continued)

Reagent added	Surface capping agent	Reaction condition	$\lambda_{\text{ex}}$ (nm)	$\lambda_{\text{em}}$ (nm)	size (nm)	QY %	Brightness ( $M^{-1} \text{ cm}^{-2}$ )	Ref.
Me <sub>2</sub> SAuCl, NaBH <sub>4</sub> (in ethanol)	Tris(2-carboxyethyl)phosphine hydrochloride L HCl	CH <sub>2</sub> Cl <sub>2</sub> , MeOH, dark, overnight	—	—	—	—	—	187
Au(tht)Cl, triethylamine, AgNO <sub>3</sub> (CH <sub>3</sub> CN), NaBH <sub>4</sub>	9-HC ≡ C-dlso<sub>1</sub>-1,2-C <sub>2</sub> B <sub>10</sub> H <sub>11</sub> (CH <sub>2</sub> Cl <sub>2</sub> )	RT, 12 h, dark	550	964	2.0	—	—	188
Au <sub>28</sub> (methanol)	—	RT, 48 h, recrystallization (layering methanol on DMF) Dark, RT, 25 h	470	1095	—	—	—	188
Ph <sub>3</sub> PAuCl (CHCl <sub>3</sub> ) & AgSbF <sub>6</sub> (methanol)	—	—	380	925	—	0.12	9.7 × 10 <sup>7</sup>	189
PhC ≡ CAu, NaBH <sub>4</sub> Me <sub>2</sub> SAuCl (CHCl <sub>3</sub> ), NaOH	1,2,3-Ph <sub>3</sub> (CN <sub>3</sub> H <sub>2</sub> ), tBuC ≡ CH	Dark, RT, 12 h	250–600	665 CH <sub>2</sub> Cl <sub>2</sub>	—	0.004	3.11 × 10 <sup>3</sup>	190
			550	625	—	0.15	1.17 × 10 <sup>5</sup>	

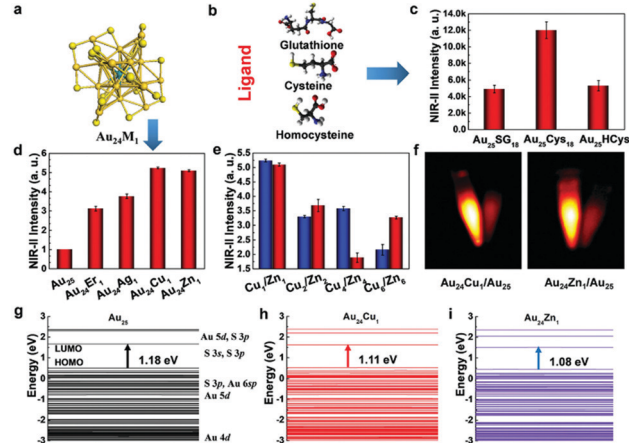


Fig. 13 (a) Cage-like crystal structure of Au<sub>25</sub> nanoclusters. Effect of (b and c) different stabilizing ligands, (d) metal doping, and (e) Cu and Zn metal doping concentration on NIR-II intensity. (f) NIR-II fluorescence images when excited at 808 nm for metal-doped Au<sub>25</sub> nanoclusters. (g-i) Changes in energy level after metal doping with respect to Au<sub>25</sub> nanoclusters using density functional theory. Reproduced with permission 176. Copyright 2019. Wiley-VCH.

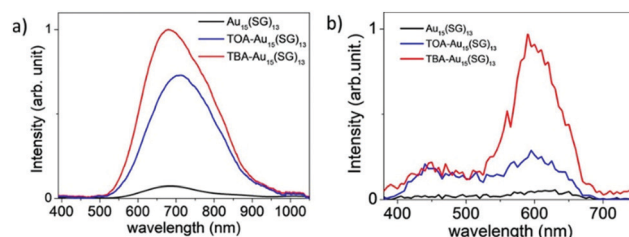


Fig. 14 One-photon excited fluorescence spectra of Au<sub>15</sub>(SG)<sub>13</sub> in (a) water and (b) presence of bulky ammonium cations, namely, tetrabutylammonium (TBA) and tetraoctylammonium (TOA) for (TOA-Au<sub>15</sub>(SG)<sub>13</sub> and TBA-Au<sub>15</sub>(SG)<sub>13</sub> in methanol). Reproduced with permission. Copyright 2018. Wiley-VCH.

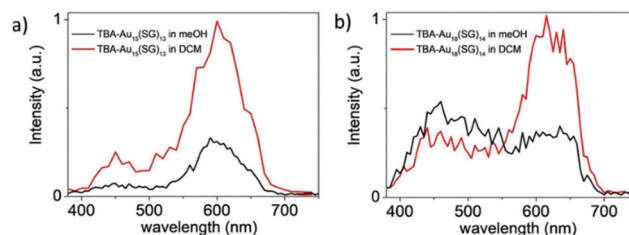


Fig. 15 Two-photon excited fluorescence spectra for (a) TBA-Au<sub>15</sub>(SG)<sub>13</sub> and (b) TBA-Au<sub>18</sub>(SG)<sub>14</sub> at the excitation wavelength of 780 nm. Reproduced with permission. Copyright 2018. Wiley-VCH.

synthesis in the Au:ligand ratio of 1:3 in the presence of NaOH. This methodology is useful for synthesizing polymer-stabilized AuNCs, exhibiting a long lifetime and excellent colloidal stability over a wide pH range and NaCl and glutathione concentration.

Recently, the preparation of DSPE-PEG [(1,2-distearoyl-sn-glycero-3-phosphoethanolamine-N-[amino(polyethylene glycol)]-encapsulated benzyl mercaptan-stabilized AuNCs was reported by Li *et al.*<sup>186</sup> The synthesis involves two steps, firstly the synthesis of benzylmercaptan (BM)-stabilized AuNCs, and then their encapsulation in amphiphilic polymer using the solvent evaporation method. Tetraoctylammonium bromide (TOAB), a phase-transfer reagent, and gold chloride salt were stirred in the presence of PhC<sub>2</sub>H<sub>4</sub>SH and NaBH<sub>4</sub>. PhC<sub>2</sub>H<sub>4</sub>SH was added to the reaction mixture again after centrifugation and stirred at room temperature to obtain BM-AuNCs. DSPE-PEG encapsulated BM-stabilized AuNCs showed enhanced PL due to aggregation-induced emission.

**3.1.1.4 Phosphorous-stabilized AuNCs.** [Au<sub>25</sub>(SR)<sub>18</sub>]<sup>-</sup> is also known as magic clusters because of its well-defined molecular structure, good stability, photoluminescence and electrochemiluminescence in the visible to near-infrared region and chiral and magnetic properties. Lei *et al.* developed the cluster from cluster approach to synthesize Au<sub>25</sub> nanoclusters from Au<sub>13</sub>, as shown Fig. 16. This synthetic approach consisted of a two-step reaction.

Firstly, [Au<sub>13</sub>{P(CH<sub>2</sub>CH<sub>2</sub>COOH)<sub>3</sub>}<sub>8</sub>Cl<sub>4</sub>]<sup>+</sup> was synthesized by dissolving tris(2-carboxyethyl)phosphine hydrochloride, L-HCl, and Me<sub>2</sub>SAuCl in a CH<sub>2</sub>Cl<sub>2</sub> and MeOH mixture, and then sodium borohydride was added when the reaction mixture turned colorless. Further, in the second step, Au<sub>13</sub> nanoclusters and polymeric (AuSR)<sub>x</sub> complexes were directly reduced in the presence of sodium borohydride and RSH at room temperature in the air, resulting in the high-yield and large-scale synthesis of [Au<sub>25</sub>(SR)<sub>18</sub>]<sup>-</sup>.<sup>187</sup>

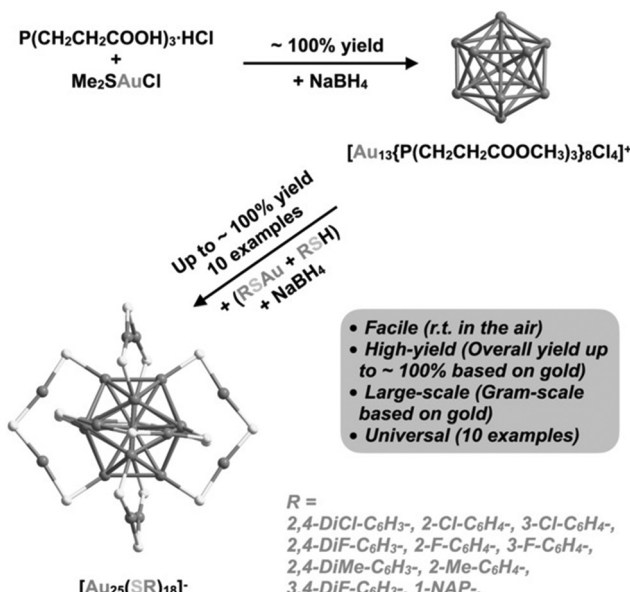


Fig. 16 Schematic illustration of cluster from cluster approach for the synthesis of AuNCs. Reproduced with permission.<sup>187</sup> Copyright 2021. Wiley-VCH.

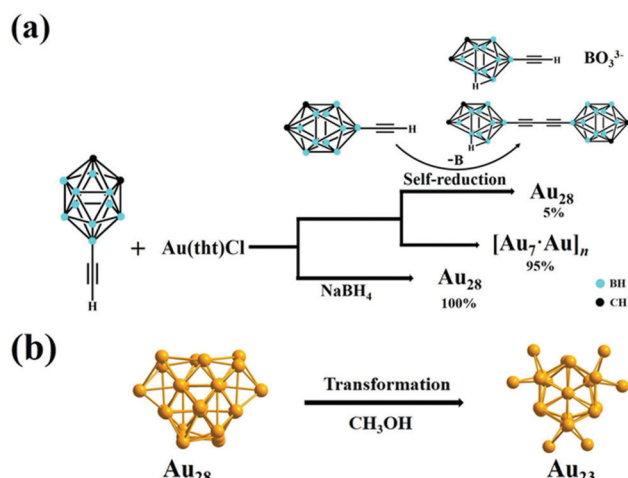


Fig. 17 Synthesis of (a) Au<sub>28</sub> nanoclusters via the self-reduction method and in the presence of sodium borohydride and (b) Au<sub>23</sub> nanoclusters from Au<sub>28</sub> in methanol. Reproduced with permission.<sup>188</sup> Copyright 2021. Wiley-VCH.

**3.1.1.5 Alkynyl-stabilized AuNCs:** Recently, the synthesis of alkynyl-protected AuNCs, their structural determination and optical properties have gained much attention. Wang *et al.* reported the preparation of the carboranealkynyl-protected gold nanocluster Au<sub>28</sub> using the self-reduction method.<sup>188</sup> The detailed reaction conditions are presented in Table 3, and as shown in the scheme in Fig. 17(a), yellow-colored [Au<sub>7</sub>-Au]<sub>n</sub> crystals were formed, which after remaining undisturbed, converted into red block crystals of Au<sub>28</sub>. The dissociated B atom was converted to BO<sub>3</sub><sup>3-</sup>, as confirmed by the <sup>11</sup>B NMR spectrum, and the Au cation was reduced to Au<sup>0</sup> together with the formation of deboronated species and coupling diyne. The yield of Au<sub>28</sub> could be improved by adding a strong reducing agent such as sodium borohydride. Given that Au<sub>28</sub> is labile in solution, it recrystallized and transformed to Au<sub>23</sub> in methanol at room temperature, as shown in Fig. 17(b).

Wan *et al.* reported NIR-emissive alkynyl-stabilized AuNCs having the formula [Au<sub>24</sub>(C≡CPh)<sub>14</sub>(PPh<sub>3</sub>)<sub>4</sub>](SbF<sub>6</sub>)<sub>2</sub>.<sup>189</sup> Han *et al.* reported alkynyl-protected Au<sub>22</sub>(tBuC≡C)<sub>18</sub> AuNCs using NaOH, showing a temperature-dependent emissive property.<sup>190</sup> Emission and excitation were available both in solution and solid state.

**3.1.1.6 Brightness of AuNCs.** Gold nanoclusters have been used for biomedical applications for a long time for fluorescence imaging because of their advantageous properties such as biocompatibility, photostability, long lifetime, and enhanced permeability and retention time. However, their poor quantum yield and low molar absorption coefficient are important issues that impact their brightness.<sup>191</sup> Thus, it is necessary to develop new synthetic approaches in the field of nanotechnology to obtain gold nanoclusters with improved brightness especially for fluorescence-based bioimaging purposes.<sup>158</sup>

Most of the synthesized gold nanoclusters have low brightness compared to conventional organic fluorophores. In earlier

reports by Cantelli *et al.*, they compared the photophysical properties of different glutathione-stabilized gold nanoclusters including  $\text{Au}_{10}(\text{SG})_{10}$ ,  $\text{Au}_{15}(\text{SG})_{13}$ ,  $\text{Au}_{18}(\text{SG})_{14}$ ,  $\text{Au}_{22}(\text{SG})_{16}$ ,  $\text{Au}_{22}(\text{SG})_{17}$ ,  $\text{Au}_{25}(\text{SG})_{18}$ ,  $\text{Au}_{29}(\text{SG})_{20}$ ,  $\text{Au}_{33}(\text{SG})_{22}$ , and  $\text{Au}_{39}(\text{SG})_{24}$ . They reported  $\text{Au}_n(\text{SG})_m$  NCs ( $n < 15$ ,  $n > 29$ ) with a low molar absorption coefficient in the order of  $10^4 \text{ M}^{-1} \text{ cm}^{-1}$  compared to organic dyes.<sup>158</sup> Fluorophore organic dyes are reported with brightness of  $10^5 \text{ M}^{-1} \text{ cm}^{-1}$  or more.<sup>192</sup> We have calculated the brightness of gold nanoclusters using the formula (brightness =  $\varepsilon_\lambda \Phi$ ), as given in the Table 3, where the molar absorption coefficient,  $\varepsilon_\lambda$ , was either calculated using the absorbance intensity/nanoparticle molar concentration or taken from the literature for glutathione-stabilized gold nanoclusters by Cantelli *et al.*<sup>158</sup> The nanoparticle concentration was calculated using the theoretically reported method by Lewis *et al.*<sup>193</sup> The brightness values were found to vary approximately in the range of  $10^{-3}$  to  $10^7$ . In most cases, the brightness values were found to be either very low or comparable to that of organic dyes.

### 3.2 Emissive Au nanoparticles (AuNPs)

In general, larger AuNPs do not show emission properties. However, within the last two decades, a few attempts successfully showed emission from AuNPs. In 2005, Luong and coworkers compared the fluorescence intensity of cetyltrimethylammonium bromide (CTAB)-stabilized longer nanorods (aspect ratio = 13) with a shorter GNR (aspect ratio = 2–3) prepared *via* an electrochemical technique. They demonstrated that the PL intensity increases several folds by increasing the aspect ratio.<sup>194</sup> In 2008, Ren and coworkers synthesized typical citrate-stabilized emissive AuNPs (16–55 nm), where the emission intensity at 610 nm ( $\lambda_{\text{ex}} = 532 \text{ nm}$ ) is directly proportional to the particle size.<sup>195</sup> The synthetic procedure involves the addition of citrate solution of different concentrations to a refluxing solution of  $\text{HAuCl}_4$ . A few years later, Negro and coworkers demonstrated lithographically engineered Au nanocylinders in a planar arrangement with both monomeric and dimeric forms on a fused silica substrate. It was observed that the PL position and the line width are related to both AuNP size and the interparticle separation between the fabricated system.<sup>196</sup>

In 2017, our group reported a simple synthetic procedure for the development of AIE from AuNPs in the NIR range in the absence of an organic fluorophore molecule (Fig. 18A).<sup>197</sup> We synthesized AuNPs *via* different procedures and treated them with diluted aqua regia, which induced the aggregation of the AuNPs (Fig. 18B), leading to the generation of an NIR luminescence peak at 916 nm upon excitation at 560 nm (Fig. 18C). In another trial, we utilized non-emissive porous-based cryptands as the aggregation source of AuNPs. The treatment of AuNPs separately with regioisomeric cryptands resulted in the generation of spherical and elongated dodecahedron gold suprastructures, which also possessed a similar emission in the NIR region.<sup>198</sup>

In our recent report, we also showed the room temperature *in situ* synthesis of luminescent gold–zinc oxide nanocomposites (Fig. 19A) in aqueous medium from the growth of AuNPs as seeds, sodium citrate as the stabilizing agent and Zn powder

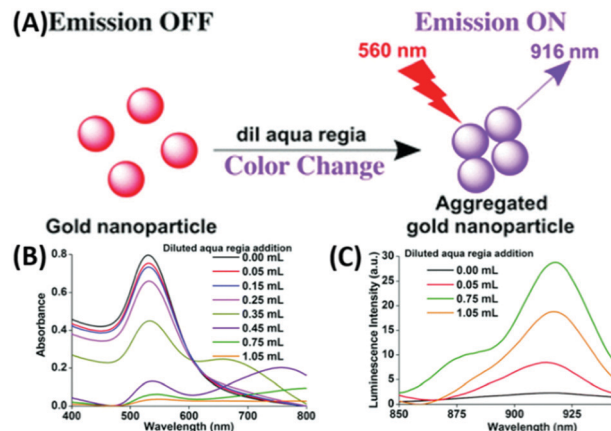


Fig. 18 (A) Synthetic scheme for luminescent AuNPs. Changes in (A) absorption and (B) increase followed by decrease in the PL intensities at 916 nm ( $\lambda_{\text{ex}} = 560 \text{ nm}$ ) due to the addition of diluted aqua regia to 3 mL of 0.6 nM AuNPs. Reproduced from ref. 197 with permission from The Royal Society of Chemistry, Copyright 2017.

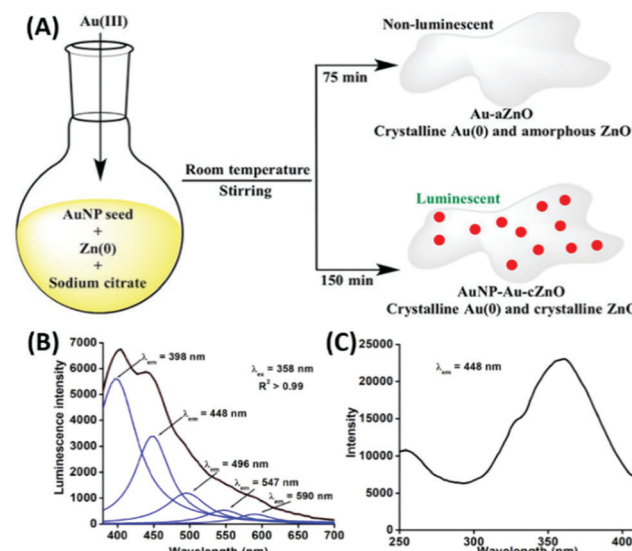


Fig. 19 (A) Synthetic route of Au-aZnO (aZn1–aZn8) and AuNP-Au-cZnO (cZn1–cZn4) nanocomposites in aqueous medium. (B) Emission and (C) excitation spectra of cZn2. Reproduced from ref. 199 with permission from Frontiers, Copyright 2021.

as the reducing agent for  $\text{Au}^{3+}$  ions added to the growth solution.<sup>199</sup> The broad emission (Fig. 19B) is due to the presence of ZnO and freshly generated 5–6 nm AuNPs on the surface of the nanocomposite.

### 3.3 Gold-based bimetallic or alloy nanoclusters

The most popular synthetic methodologies for NPs involve the top-down and bottom-up approaches.<sup>98</sup>

The luminescent properties in BMNCs appear due to their distinct synergistic<sup>145</sup> and relativistic<sup>139</sup> effects, which diversify their utility in numerous fields. Hence, controlled doping of one metal is very challenging in the presence of another metal. Mostly, the chemical reduction methods have been utilized to



synthesize BMNCs. Other classification parameters, which involve the synthesis of BMNC, are based on the type of synthetic procedures, type of metals, protecting ligands used or based on metal precursors.<sup>109,200,201</sup> Another way to specifically classify the bimetallic system is based on the type of chemical reduction utilized in the procedure. If both metal precursors get reduced *via* one-pot synthesis, it is known as co-reduction synthesis, which generally originates from their monometallic procedures.<sup>201</sup> In contrast, the other method includes post-synthetic modification constituting two steps. Firstly, the procedure involves the synthesis of intermediary monometallic NCs followed by post-synthetic treatment to get

BMNCs by introducing the second metal ion.<sup>201,202</sup> In this review, we classify gold-based BMNCs firstly based on the metal precursors utilized in the system, followed by the ligands utilized to separate them. The preparation of gold-based BMNCs typically involve the combination of gold with the other two coinage metals.

**3.3.1 Au–Ag BMNCs.** Among the bimetallic noble metal NCs, Au/Ag BMNCs are the most explored case. To provide better stabilization of BMNCs, we classified them into different sections based on the ligands used in their synthesis. A brief idea about the regents and reaction conditions are presented in Table 4.

Table 4 Au–Ag NCs

Reagents added	Surface capping agent	Reaction condition	Au:Ag	$\lambda_{\text{ex}}$ (nm)	$\lambda_{\text{em}}$ (nm)	Size (nm)	QY%	Ref.
NaOH, NaBH <sub>4</sub>	BSA	RT	1:1	370	707	1.2	2.8%	142
NaOH	BSA	37 °C, 12 h	25:6	370	620	4.5 <sup>a</sup>	10.5%	143
NaOH, NaBH <sub>4</sub>	BSA	37 °C, 20 h	2.3:2	490	718	~2	42%	203
NaOH	BSA	30–70 °C & 30 to 300 min	6:1	420	645	~2.35	17.6%	205
NaOH	BSA	37 °C, 6 h	7:1.7	325	405	2.1 ~ 4.2	NA	206
NaOH	BSA	37 °C, 12 h	1:1	390	630, 470	~3–5	6.37	207
NH <sub>3</sub> ·H <sub>2</sub> O	BSA	700 W, 3 min	6:1	365	577	~3–5	6.8%	208
NaOH	Lipoic acid	70 °C, 8 h	5:1	385	630	1.9 ± 0.4	6.4%	209
NA	GSH	70 °C, 24 h	1:0.2	335	605	~2 nm	7.2%	211
NA	GSH	65 °C, 48 h	47:1	400	600	1.78 ± 0.20	13%	212
NA	GSH	RT, 12 h	1:1	320	515, 630	1.7 ± 0.4	26%	213
NaOH	GSH	80 °C, 3 h	3:2	360	616, 412	~1	NA	214
NaOH	GSH	RT, 1.5 h, inert atm.	9:1	370	610	<2	9.6%	215
NaBH <sub>4</sub>	GSH	20 °C, 15 h	3:1	520	680 <sup>1</sup> , 710 <sup>2</sup> , 815 <sup>3</sup>	0.43 <sup>1</sup> , 0.65 <sup>2</sup> , 0.76 <sup>3</sup>	NA	216
Ag NC	MSA	RT, 5 h	NA	390	650	NA	0.035	217
NA	11-MUA	RT, 5 h	variable	285–355	607–635	~1.5	6.18%	218
NaOH	11-MUA	RT, 20 min	4:1	320	610	1.56	NA	219
NaOH, NaBH <sub>4</sub>	11-MUA	15 min	variable	250–330	608–640	1.8–2.1	NA	220
PEG	MUTB	70 °C, 5 h	variable	353–397	440–455, 620–665	< 2 min	NA	221
NA	DAMP	70 °C, 5 h	1:1	473	640	1.63 ± 0.4	42.4	222
Dopamine	Chondroitin sulfate	30 °C, 4 h	1.5:1	450	510	0.99	1.41	223
AuNP, AA	CTAC	60 °C, 1 h	NA	820	650–700 (2PPL)	20–25	NA	152
DNA-AgNCs, NaBH <sub>4</sub>	5'-CCCTTAATCCCC-3', 5'-CCCCCCCCCCC-3', and 5'-CCCTCTTAACCC-3'	Ice bath, 30 min	1:1	460	630	NA	4.5	223
NaBH <sub>4</sub>	5'-CGCCCCCTTGGCGT-3'	Ice bath, 15 min	1:1	260	605	2.75	NA	224
NA	C4-ATAT-C4	80 °C, 1 h	1:1	290	535	8.3	0.78	225
NA	Cytidine	80 °C	1:1	370	560	1.50 ± 0.31	9%	226
Sodium citrate	AMP	120 °C, 30 min	1:5	354	550	2.25	8.46%	227
Sodium citrate	AMP	80 °C, 6 h	9:1	356	475	1.25	9.42%	228
NaOH	Lysozyme	37 °C, 22 h	5:1	420	660	1.75	4.5%	229
NA	L-Tryptophan	120 °C, 4 h	1:10	370	455	2.7	20%	230
NaOH	Methionine	37 °C, 10 h	2:1	526	756	5	NA	231
NaOH	Egg white protein	250 W, 90 °C, 250 psi, 30 min	1:8	360	600	4.4	5.4%	232
NA	Egg shell membrane	RT, 3/7 days	1:1	340	435–445	5–100	NA	233
p(NIPAM-AA-AAM)-Ag hybrid microgels	Ascorbic acid	Ice bath, 38 min	NA	236	370	NA	NA	234
Au@PNIPAM microgels	CTAB, ascorbic acid	RT	Variable	405	570–580	~57–102	NA	236
[Au <sub>11</sub> (PPh <sub>3</sub> ) <sub>8</sub> Cl <sub>2</sub> ] <sup>+</sup> NaSbF <sub>6</sub>	PhC <sub>2</sub> H <sub>4</sub> SAg	RT, 6 h	NA	370	680	NA	40.1%	135
C <sub>18</sub> H <sub>15</sub> AuClP	BDT, TPP, NaBH <sub>4</sub>	Dark, 12 h	2:3	~445	~660	NA	24%	136
Ag <sub>25</sub> (SPhMe <sub>2</sub> ) <sub>18</sub>	AuCLPPh <sub>3</sub>	RT, 4 h	NA	467	~810	NA	NA	237
NaBH <sub>4</sub>	Lipoic acid	RT, 3–5 h	1:1	485	~680	NA	7.9%	202
Ag <sub>25</sub> (SPhMe <sub>2</sub> )PPh <sub>4</sub>	AuCLPPh <sub>3</sub>	RT, 4 h	NA	405	810	NA	NA	145

<sup>a</sup> Indicates hydrodynamic diameter.<sup>1, 2</sup> and <sup>3</sup> corresponds to 3 different NCs ↑ represents increase in PL intensity. The brightness could not be calculated for BMNCs due to the difficulties faced during the calculation of the concentration of NCs which involve radius of both metals.



**3.3.1.1 BSA-mediated Synthesis:** During the last decade, BSA protein remains the most frequent choice during the synthesis of BMNCs. This is due to the presence of residues such as cysteine, which not only can reduce  $\text{Au}^{3+}$  but also stabilize the  $\text{Au}(0)$  clusters by the formation of a strong Au-S bond.

T. Pradeep and co-workers first introduced BSA for the preparation of luminescent  $\text{Au}/\text{Ag}$  alloy NCs (1.2 nm), which were obtained by gently mixing and stirring the separately synthesized BSA-capped  $\text{Au}_{38}$  and  $\text{Ag}_{31}$  quantum clusters (QC) (Fig. 20). In another galvanic exchange method, different concentrations of aq.  $\text{Au}^{3+}$  were introduced in the as-prepared  $\text{AgQC@BSA}$  under vigorous stirring and the reaction continued for 8 h to yield  $\text{Au}/\text{Ag}$  BMNCs.<sup>142</sup> Upon excitation 370 nm, the  $\lambda_{\text{em}}$  of these BMNCs red-shifted to 707 nm, unlike the  $\text{AuQCs}$  and  $\text{AgQCs}$ , having  $\lambda_{\text{em}}$  at 660 and 670 nm, respectively. Inspired by this, K. Chattopadhyay and co-workers also synthesized red-emissive  $\text{Au}-\text{Ag}@\text{BSA}$  NCs by simply adding  $\text{Au}^{3+}$  and  $\text{Ag}^+$  to BSA solution and stirring at 37 °C for 20 h. However, increasing the dopant (Ag) concentration caused a continuous red shift in the emission maximum, which is mainly attributed to the modulation of the electronic state with silver doping. Another possible explanation is either the presence of MLCT

( $\text{M} \rightarrow \text{BSA}$ ) or MMCT ( $\text{Ag} \rightarrow \text{Au}$ ) in the BMNCs. The molar ratio of  $\text{Au}:\text{Ag}$  was optimized to 2.3:2.0 at an effective pH of 11 to obtain enhanced emissive  $\text{Au}-\text{Ag}@\text{BSA}$ , which was subsequently utilized for the cellular detection of toxic heavy metals ( $\text{Pb}^{2+}$ ).<sup>203</sup>

It was reported that the tyrosine residues present in BSA can reduce  $\text{Au}^{3+}$  to  $\text{Au}(0)$  in basic medium with  $\text{pH} > 9$ . Hence, the basic medium was utilized to synthesize BSA-mediated AuNCs.<sup>204</sup> For instance, Zhang *et al.* reported the synthesis of bimetallic alloying  $\text{Au}-\text{AgNCs}$  by utilizing metal precursor  $\text{HAuCl}_4$  and  $\text{AgNO}_3$  with BSA functioning as both the reducing and stabilizing agent in basic medium.<sup>143</sup> By maintaining the molar ratio of  $\text{Au}:\text{Ag}$  precursors to 25:6 in the reaction medium, this silver effect exceptionally enhanced the red emission (620 nm) intensity of the  $\text{Au}-\text{AgNCs}$  by several folds compared to that of conventional AuNCs and core shell  $\text{Au}@\text{AgNCs}$ .

XPS studies confirmed not only the presence of  $\text{Au}(0)$  and  $\text{Ag}(0)/\text{Ag}(i)$  but also confirmed the Au-S interaction, which suggest that the formation and attachment of bimetallic  $\text{Au}-\text{AgNCs}$  in the S-containing site of the protein scaffold is the probable path of nucleation in the protein scaffold. BMNPs initiate with the reduction of  $\text{HAuCl}_4$  and  $\text{Ag}^+$  ions by 21 tyrosine residues in the protein scaffold. The competitive nucleation rate is faster in  $\text{Au}$  than  $\text{Ag}$ . Hence, after nucleation, these  $\text{Au}$  atoms catalytically enhance the  $\text{Ag}$  deposition in the protein matrix and their co-deposition leads to the formation of bimetallic  $\text{Au}-\text{AgNCs}$ . The origin of luminescence was attributed to the presence of LMCT in the BMNCs. In addition, the silver effect specifically enhanced the sensing performance of the  $\text{Au}-\text{AgNCs}$  towards different metal ions such as  $\text{Cu}^{2+}$  and  $\text{Hg}^{2+}$ . There are a few other reports available on the synthesis of  $\text{Au}-\text{AgNCs}$  following a similar method with minor modifications.<sup>205,206</sup>

In another discovery, K. Huang and co-workers reported BSA-protected dually emissive  $\text{Au}-\text{AgNCs}$  through a green synthetic procedure, which involved the addition of an aqueous solution of  $\text{HAuCl}_4$  and  $\text{AgNO}_3$  to a BSA solution with a gentle stirring for 2 min, followed by the addition of  $\text{NaOH}$  solution at 37 °C.<sup>207</sup> As shown in Fig. 21, the BSA-stabilized  $\text{Au}-\text{AgNCs}$  possess dual emission peaks at 470 nm ( $\text{Ag NCs}$ ) and 630 nm ( $\text{Au NCs}$ ) under 390 nm excitation. These emissions may originate from the different interactions of the metal core with the surface ligand.

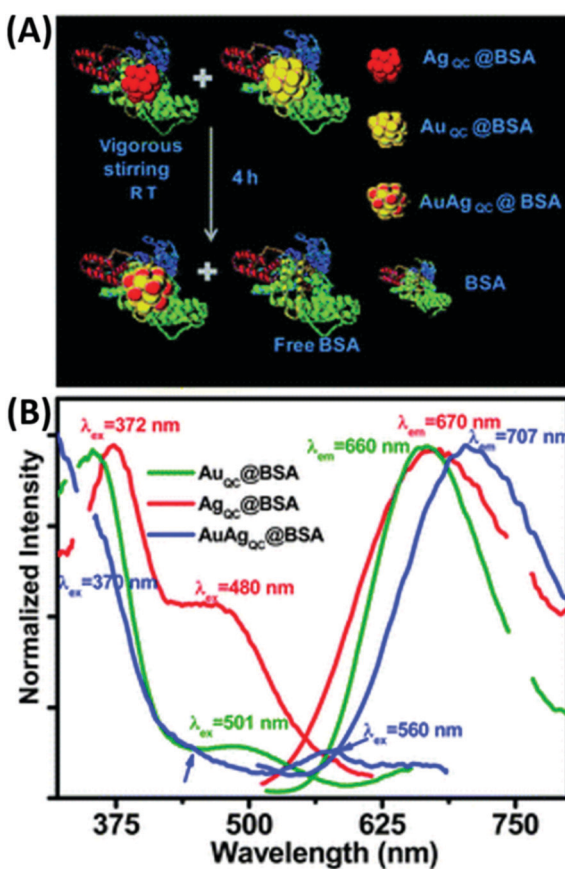


Fig. 20 (A) Synthetic scheme of  $\text{AuAg}@\text{BSA}$  alloy clusters through QC-QC interaction and (B) emission spectra of  $\text{AuQC}$ ,  $\text{AgQC}$  and  $\text{AuAgQC}@\text{BSA}$  indicated by green, red, and blue line, respectively.  $\lambda_{\text{ex}} = 370 \text{ nm}$ . Reproduced from ref. 142 with permission from The Royal Society of Chemistry, Copyright 2012.

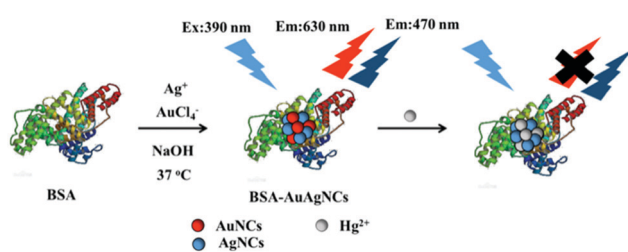


Fig. 21 Schematic illustration of the synthesis of dual-emitting BSA-Au/Ag NCs and their application towards  $\text{Hg}^{2+}$  sensing. Reproduced with permission from ref. 207, Copyright Elsevier (2018).



The origin of the emissive properties is attributed to the perturbation of the electronic state in the quantum confinement region. Upon interaction with  $\text{Hg}^{2+}$ , the luminescence intensity at 630 nm quenched due to the high-affinity of  $\text{Hg}^{2+}$  towards  $\text{Au}^+$  *via*  $\text{d}^{10}-\text{d}^{10}$  metallophilic interaction. BSA-protected Au–Ag luminescent BMNCs were also synthesized by Zheng *et al.* *via* a simple microwave (MW)-assisted method. The BSA solution was added to a mixture containing an aqueous solution of  $\text{HAuCl}_4$  and  $\text{AgNO}_3$  under stirring condition followed by the addition of  $\text{NH}_3\cdot\text{H}_2\text{O}$ . Heating by MW radiation yielded yellow emissive (577 nm) bimetallic Au/Ag NCs.<sup>208</sup>

**3.3.1.2 Sulfur-containing Ligand-mediated Synthesis:** The interaction of thiol with noble metals is well established due to their soft–soft interactions. Researchers across the world utilized this fact to explore different synthetic methods for noble metal NCs by simply employing sulfur-containing ligands in the reaction medium. For example, Huang *et al.* utilized the strong Au and Ag interaction with sulfur to synthesize fluorescent Au–AgNCs by employing lipoic acid as a capping agent.<sup>209</sup> Lipoic acid is dissolved in a strongly basic solution followed by the addition of  $\text{HAuCl}_4$  and  $\text{AgNO}_3$  solution in a molar ratio of 5:1 under constant stirring at elevated temperature (Fig. 22A). Further centrifugation yielded red-emitting (630 nm) Au–Ag BMNCs, where the luminescence intensity was highly dependent on temperature and decreased with an increase in temperature from 20 °C to 65 °C (Fig. 22B).<sup>209</sup> This phenomenon is attributed to the increase in the rate of collision frequency, which eventually results in increased non-radiative transition with an increase in temperature without affecting the radiative transition rate. The as-prepared Au–Ag BMNCs were reported as a chemosensor for  $\text{Fe}^{3+}$  through aggregation-induced quenching of the parent BMNPs.

The origin of the aggregation is attributed to the interaction of  $\text{Fe}^{3+}$  with the carboxylate group of lipoic acid (Fig. 22C). Hikosou *et al.*, Brach *et al.* and Ye *et al.* separately synthesized

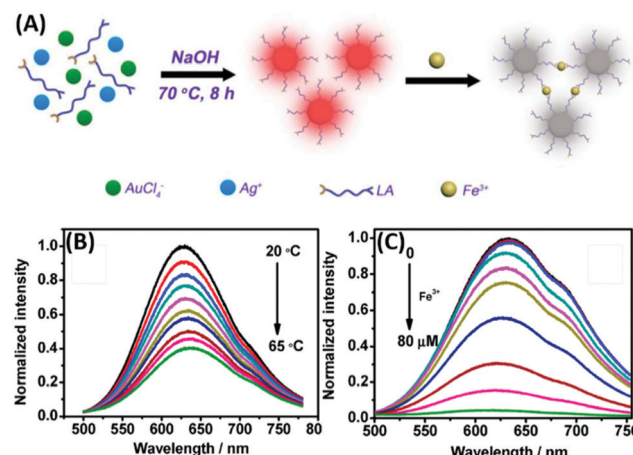


Fig. 22 Schematic illustration of the (A) synthesis of lipoic acid-stabilized Au/Ag BMNCs and their  $\text{Fe}^{3+}$  sensing and (B) temperature- and (C)  $\text{Fe}^{3+}$ -dependent fluorescence quenching. Reproduced with permission from ref. 209, Copyright Elsevier (2016).

GSH-stabilized bimetallic luminescent Au–AgNCs by modifying the Au:Ag ratio in the synthetic procedure.<sup>210–212</sup> Liu *et al.* also synthesized dual-emitting GSH-stabilized Au–AgNCs by reacting GSH,  $\text{AgNO}_3$  and  $\text{HAuCl}_4$  in basic medium for 6 h at 80 °C.<sup>213</sup> The as-synthesized NCs exhibited emission bands at 412 nm and 616 nm upon excitation at 360 nm. This nanosystem was demonstrated as a potential ratiometric fluorescence probe for the detection of Arg and Cys amino acids. Yin *et al.* also followed a similar procedure to obtain orange-emitting Au–AgNCs by maintaining the Au:Ag molar ratio at 9:1.<sup>214</sup> Yao and co-workers synthesized GSH-stabilized Au–Ag BMNCs by reacting a 3:1 molar ratio of Au:Ag with excess GSH in methanol. The reduction of the metal precursors was carried out using sodium borohydride under an inert atmosphere.<sup>215</sup>

T. Pradeep and co-workers introduced mercaptosuccinic acid towards the synthesis of emissive BMNCs. The detail multi-step procedure involves the synthesis of MSA-stabilized AgNPs, which produced AgNCs through interfacial etching. The next step included the addition of  $\text{HAuCl}_4$  to the pre-synthesized  $\text{Ag}_{7/8}$  cluster with gentle stirring to get the resultant emissive  $\text{Ag}_7\text{Au}_6$  alloy NCs.<sup>216</sup> Jin and co-workers employed MUA as another thiol-containing capping agent to synthesize luminescent MUA–Ag/Au BMNCs with an emission peak at 630 nm.<sup>217</sup> It was observed that the emission wavelength varied with the amount of Ag doping, but was independent of the excitation wavelength. While a similar reaction was performed by Yang *et al.* in basic medium,<sup>218</sup> Ristig *et al.* utilized  $\text{NaBH}_4$  to complete the reduction process to get the desired product.<sup>219</sup>

T. Yonezawa and co-workers utilized the double-target sputtering method to synthesize bimetallic Au/Ag nanoclusters by utilizing 11-mercaptopentadecyl-*N,N,N*-trimethylammonium bromide (MUTAB) as the surface-protecting ligand. Both Au and Ag metal targets were employed in the usual sputtering process and etched simultaneously by ionized Ar gas under high vacuum. The targets were set to face each other at a certain angle, enabling the generated unstable Au and Ag particles to have a higher collision probability, which resulted in the formation of Au–Ag BMNCs.<sup>220</sup> By introducing a new sulfur-containing capping agent, 4,6-diamino-2-mercaptopurine (DAMP), Yu *et al.* synthesized luminescent Au–Ag NCs in a one-pot synthetic method and utilized them for the detection of  $\text{Hg}^{2+}$  (Fig. 23A–C).<sup>221</sup>

**3.3.1.3 Templated synthesis.** Q. Liu *et al.* utilized chondroitin sulphate as new sulfur-containing template for the synthesis of novel fluorescent bimetallic Au/Ag NCs by simply reacting  $\text{AgNO}_3$  and  $\text{HAuCl}_4$  with a chondroitin sulphate solution. After 30 min of stirring, a dopamine solution was introduced in the reaction mixture, followed by stirring, resulting in a reddish-brown color solution containing Au/Ag NCs with an emission at 610 nm, which is attributed to the synergistic effect arising in the presence of silver.<sup>222</sup> P. Yuan *et al.* synthesized bimetallic core-shell Au@Ag NPs possessing two-photon PL by utilizing cetyltrimethylammonium chloride solution (CTAC) as the template. They successfully demonstrated a two-photon PL (2PPL) enhancement with an increase in the Ag shell thickness.<sup>152</sup>

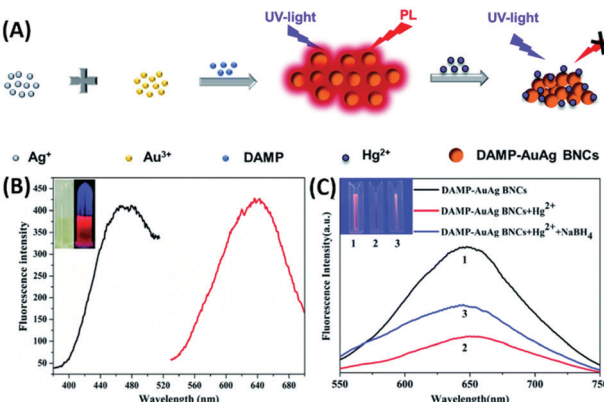


Fig. 23 (A) Schematic illustration of synthetic process of DAMP-AuAg BMNCs and mercury ion-induced fluorescence quenching. (B) Excitation (black line) and emission (red line) spectra of the DAMP-AuAg BMNCs. Inset: DAMP-AuAg BMNC solution under visible light and UV at 365 nm. (C) Fluorescence spectra ( $\lambda_{\text{ex}} = 473$  nm). Inset: Picture of DAMP-Au-Ag BMNCs under UV light in the (1) absence and (2) presence of  $\text{Hg}^{2+}$  ions (50  $\mu\text{M}$ ), and (3) solution (2) after the addition of aqueous  $\text{NaBH}_4$  (10 mM). Reproduced from ref. 221 with permission from The Royal Society of Chemistry, Copyright 2021.

**3.3.1.4 Biomolecule-mediated synthesis.** Biomolecules such as DNA, peptides and amino acids assisting the synthesis of luminescent bimetallic Au/Ag NCs have attracted special attention given that the complex structural property of biomolecules induces the resultant shape during the growth of NCs. For example, in 2011 Chang and co-workers synthesized DNA (5'-CCCTTAATCCCC-3' or 5'-CCCCCCCCCCCC-3' or 5'-CCCTTAAACCC-3')-assisted Au/Ag BMNCs by reacting the DNA molecule with both metal precursors (DNA: Au: Ag = 1:6:6) in an ice bath for 15 min in the presence of  $\text{NaBH}_4$  as a reducing agent.<sup>223</sup>

Similarly, Pang and co-workers replaced the DNA sequence to 5'-CGCCCCCTGGCGT-3' in the previous procedure to get red-emissive DNA-assisted Au/Ag BMNCs.<sup>224</sup> Deng and co-workers synthesized DNA-mediated emissive Au-Ag BMNCs by adding  $\text{HAuCl}_4$  and  $\text{AgNO}_3$  to DNA molecules in citrate-citric acid buffer.<sup>225</sup> Wang and co-workers introduced the cytidine-template synthesis of luminescent bimetallic cytidine-AuAg NCs. Specifically, to a cytidine solution in PBS buffer, an aqueous solution of  $\text{HAuCl}_4$  was introduced, followed by citrate buffer (pH 6). The reaction mixture was heated in a water bath at 80 °C followed by the addition  $\text{AgNO}_3$  to yield bimetallic cytidine-AuAg NCs with an emission centered at 560 nm.<sup>226</sup>

In 2017, Wu and co-workers introduced for the first time for the hydrothermal synthesis of fluorescent bimetallic Au-Ag NCs@AMP using adenosine monophosphate (AMP) as the surface-protecting ligand. The AMP (solid) in deionized water together with  $\text{HAuCl}_4$ ,  $\text{AgNO}_3$  and sodium citrate solution (Au: Ag: AMP to 0.2:1:5) was autoclaved at 120 °C to get the emissive BMNCs. Similar BMNCs were also prepared by two other methods involving heating and stirring *via* seed-mediated hydrothermal synthesis.<sup>227</sup> By modifying the Au: Ag to 9:1,

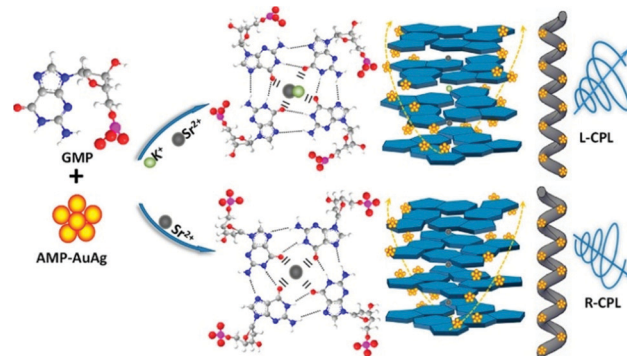


Fig. 24 Schematic illustration of the self-assembly of g-fiber-AuAg NCs exhibiting R-/L-CPL emission. Reproduced from ref. 228 with permission from the American Chemical Society, Copyright 2020.

Z. Suo *et al.* also synthesized AMP-Au/Ag NCs and incorporated them in pre-synthesized right and left handed G-quartet nanofibers to obtain enantiomeric circularly polarized light emission (Fig. 24).<sup>228</sup>

S. Pang *et al.* carried out the reduction reaction of Au and Ag precursors in basic medium by introducing lysozymes as a stabilizing agent to get the luminescent Lys-Au/Ag BMNCs.<sup>229</sup>

Meng *et al.* synthesized L-Trp@AuAgNCs by utilizing tryptophan as a reducing and capping agent in the reaction mixture involving Au and Ag metal precursors.<sup>230</sup> Recently, Zou and co-workers synthesized methionine (Met)-stabilized Au-Ag BMNCs *via* a doping growth strategy.

The brief synthetic procedure involves mixing of  $\text{AgNO}_3$ ,  $\text{HAuCl}_4$  and Met in water under ultrasonication with a pH of 12.0. The orange-colored mixture was sealed at 37 °C for 10 h followed by the addition of a drop of  $\text{H}_2\text{SO}_4$  to precipitate the Au-Ag BMNCs.<sup>231</sup>

Chicken eggs, which are enriched with several proteins, have also been considered for the synthesis of metallic NCs. For example, Li and co-workers utilized the chicken egg white protein matrix to synthesize orange-emitting Au-Ag BMNCs *via* a microwave-assisted facile green one-pot synthetic method.<sup>232</sup> Briefly, to the egg white protein obtained after centrifugation, aqueous  $\text{HAuCl}_4$  solution followed by  $\text{AgNO}_3$  solution (varying ratio with Au) was added under vigorous stirring. Then, NaOH solution was added to the mixture under continuous shaking, and finally put in a microwave at 250 W 90 °C and 250 Psi for 30 min under stirring, yielding Au-Ag BMNCs.<sup>232</sup> Similarly, Pramanik *et al.* synthesized bimetallic alloy Au-Ag NCs in the absence of any reducing agent *via* the ESM-induced reduction of  $\text{AgNO}_3$  and  $\text{HAuCl}_4$  solutions at room temperature.<sup>233</sup>

**3.3.1.5 Polymer-mediated synthesis.** Zhou and co-workers demonstrated the *in situ* synthesis of luminescent bimetallic Ag-Au NPs by performing the reduction reaction of  $\text{Ag}^+$  in the presence of poly(*N*-isopropylacrylamide-acrylic acid-acrylamide) [p(NIPAM-AA-AAm)] microgel followed by treatment with  $\text{HAuCl}_4$  solution under stirring in an ice bath.<sup>234</sup> After the color change, L-AA was added to complete the reduction



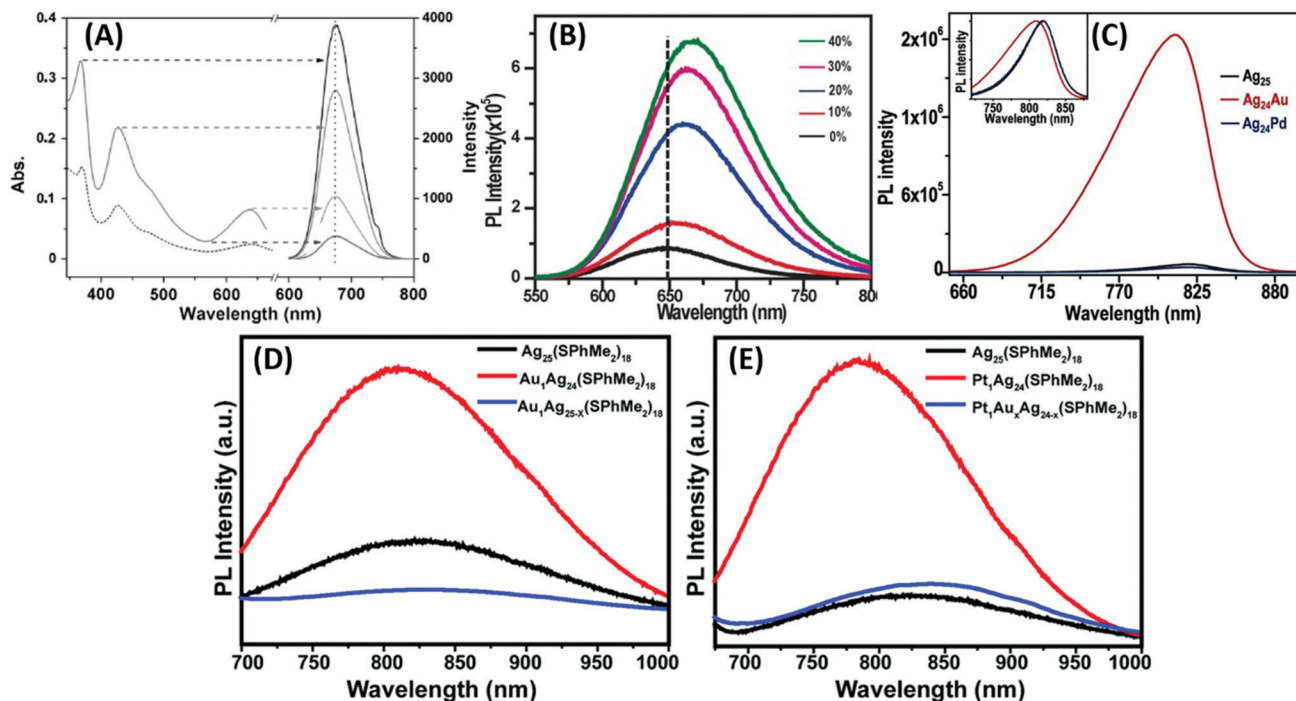
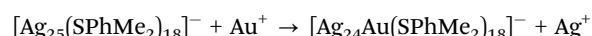


**Fig. 25** (A) Enhancement in PL intensity of product NC II  $[\text{Ag}_{13}\text{Au}_{12}(\text{PPh}_3)_{10}(\text{SR})_5\text{Cl}_2]^{2+}$ . PL (–), UV/Vis (..), UV/Vis and excitation spectra (left), and emission spectra (right) at arrow-indicated excitation wavelengths. (B) PL spectra of undoped  $\text{Ag}_{29}$  and different percentages (mmol%) of Au-doped  $\text{Ag}_{29}$  clusters. (C) PL spectra of  $[\text{Ag}_{25}(\text{SPhMe}_2)_{18}]^-$ ,  $[\text{Ag}_{24}\text{Au}(\text{SPhMe}_2)_{18}]^-$ , and  $[\text{Ag}_{24}\text{Pd}(\text{SPhMe}_2)_{18}]^{2-}$  clusters. Inset represents the normalized spectra. PL spectra of (D)  $\text{Ag}_{25}(\text{SPhMe}_2)_{18}$ ,  $\text{Au}_1\text{Ag}_{24}(\text{SPhMe}_2)_{18}$ , and  $\text{Au}_x\text{Ag}_{25-x}(\text{SPhMe}_2)_{18}$  and (E)  $\text{Ag}_{25}(\text{SPhMe}_2)_{18}$ ,  $\text{Pt}_1\text{Ag}_{24}(\text{SPhMe}_2)_{18}$ , and  $\text{Pt}_1\text{Au}_x\text{Ag}_{24-x}(\text{SPhMe}_2)_{18}$  with  $\lambda_{\text{ex}} = 405 \text{ nm}$ . (A)–(C) Reproduced with permission.<sup>135,138,237</sup> Copyright 2014. Wiley–VCH. (D) and (E) reproduced from ref. 143 with permission from The Royal Society of Chemistry. Copyright 2014.

process to get p(NIPAM-AA-AAm)–Ag/Au. Rubio-Retama and co-workers also synthesized luminescent bimetallic Au@Ag@PNIPAM having a variable silver thickness.<sup>235</sup> The detailed procedure includes the growth reaction of the as-prepared Au@PNIPAM NPs in the presence of CTAB as the template followed by AA-mediated reduction of  $\text{Ag}^+$ .

**3.3.2 Heterometal-incorporated Au or Ag NCs.** Several research attempts have been made to incorporate Ag atoms in AuNCs or *vice versa*, which increases the PL quantum yield of the resultant alloy NCs, as mentioned in Section 2.3. For example, in Fig. 6a–c, phosphine-protected  $[\text{Ag}_{12}\text{Au}_{13}(\text{PPh}_3)_{10}(\text{SR})_5\text{Cl}_2]^{2+}$  NCs (i) were prepared *via* a two-step process involving the preparation of triphenylphosphine (TPP)-stabilized monometallic  $\text{Ag}_{25}$  NCs, followed by the treatment of phenethylthiosilver ( $\text{PhC}_2\text{H}_4\text{SAg}$ ) at room temperature. The final NC I was obtained after crystallization. For the synthesis  $[\text{Ag}_{13}\text{Au}_{12}(\text{PPh}_3)_{10}(\text{SR})_5\text{Cl}_2]^{2+}$  NCs (ii), firstly, the TPP-protected previously reported procedure was employed for the synthesis of  $\text{Ag}_{29}$  NCs,<sup>236</sup> and then  $\text{Au}_{11}$  NCs were prepared, followed by their reaction with  $\text{PhC}_2\text{H}_4\text{SAg}$  at  $40^\circ\text{C}$  to get the desired product (Fig. 25A).<sup>135</sup> By modifying the doping of Au atoms,  $\text{Ag}_{29}(\text{BDT})_{12}(\text{TPP})_4$  NCs were achieved by Bakr and co-workers, who performed the  $\text{NaBH}_4$ -mediated reduction reaction of  $\text{AuClPC}_{18}\text{H}_{15}$  and  $\text{AgNO}_3$  in presence of BDT and TPP. With an increase in the Au doping, the alloy NCs showed an enhancement in emission intensity together with a red shift

in  $\lambda_{\text{em}}$  (Fig. 25B).<sup>138</sup> The same group also utilized the galvanic exchange reaction for mono gold doping in  $\text{Ag}_{25}$  NCs. The galvanic reaction involved in the reaction is as follows:



Briefly, for the synthesis of  $\text{Au}_1\text{Ag}_{24}(\text{SPhMe}_2)_{18}\text{PPh}_4$  alloy NCs, the pre-synthesized  $\text{Ag}_{25}(\text{SPhMe}_2)_{18}\text{PPh}_4$  was treated with  $\text{AuClPPh}_3$  in DCM under vigorous stirring for 4 h at room temperature to get a green-coloured solution.  $\text{AgCl}$  was removed by centrifugation and washing. The final cluster precipitate was dissolved in DCM and crystallized in a DCM/hexane mixture.<sup>237</sup> By following a previously reported procedure for the synthesis of  $\text{Ag}_{25}(\text{SPhMe}_2)_{18}$  NCs,<sup>238</sup> the same group also tried to dope more than one atom of Au and Pd inside the  $\text{Ag}_{25}$  clusters by performing the sodium borohydride-mediated reduction reaction of  $\text{AgNO}_3$  and  $\text{AuClPPh}_3/\text{Pd}(\text{OAc})_2$  together with  $\text{HPhMe}_2$  and  $\text{PPh}_4\text{Br}$ .<sup>237</sup> The doping of a single Au atom remarkably enhanced the luminescence signal up to 25-fold against Pd-doped or pure  $\text{Ag}_{25}$  NCs (Fig. 25C). The blue shift in  $\lambda_{\text{em}}$  is attributed to the Ag atom, which modulates the HOMO–LUMO gap and/or the surface states after its incorporation in the crystal structure.<sup>237</sup>

Three years later, Groot and co-workers demonstrated mono Au atom doping in  $\text{Ag}_{29}$  NCs by modifying the procedure previously reported for the synthesis of  $\text{Ag}_{29}$  NCs.<sup>202,239</sup>



The synthetic procedure involves the reduction reaction of  $\text{AgNO}_3$  followed by  $\text{HAuCl}_4$  in the presence of LA and  $\text{NaBH}_4$  at room temperature overnight. In another post-synthetic method,  $\text{Ag}_{29}$  NCs were prepared first, followed by treatment with gold chloride salt and  $\text{NaBH}_4$  under stirring overnight to get the desired product. The Au-doped AgNCs possessed enhanced PL properties, which is attributed to the feasible radiative decay.<sup>202</sup>

For the synthesis of mono Pt atom-doped  $\text{Pt}_1\text{Ag}_{24}(\text{SPhMe}_2)_{18}\text{PPh}_4$  NCs, Yuan *et al.* performed the  $\text{NaBH}_4$ -mediated reduction reaction of  $\text{AgNO}_3$  and  $\text{H}_2\text{PtCl}_6$  in solution. The precipitation of the NCs was accomplished by the treatment with excess  $\text{PPh}_4\text{Br}$ .<sup>145</sup> Mono Au-doped AgNCs were prepared using the reported procedure described in ref. 237. For the replacement of more Ag atoms by Au or Pt atoms, the previously synthesized single-atom substituted NCs,  $\text{M}_1\text{Ag}_{24}(\text{SR})_{18}$  ( $\text{M} = \text{Au}$  or  $\text{Pt}$ ) were reacted with  $\text{Me}_2\text{PhSAu}$  under stirring for 1 h. By replacing the innermost atom of  $\text{Ag}_{25}(\text{SR})_{18}$  by Au or Pt, there was a remarkable increase in the PL intensity of the mono-doped NCs compared to the undoped or multi atom doped NCs (Fig. 25D and E), respectively.<sup>145</sup>

**3.3.3 Au/Cu NCs.** Millstone and co-workers synthesized luminescent bimetallic Au–Cu nanoalloys, where the emission wavelength varied in the NIR region depending on the composition of the NPs.<sup>240</sup> Briefly, the procedure included the addition of gold and copper solution (varying percentage) to poly(ethylene glycol) methyl ether thiol (PEG-SH) followed by a color change to dark yellow. Subsequently, the co-reduction of the metals was performed by introducing  $\text{NaBH}_4$  to get the desired product.

It was observed that with an increase in the copper ratio, a bathochromic shift in the emission maximum occurred from 947 nm to 1067 nm. Chang and co-workers proposed a one-pot synthetic method for the preparation of penicillamine-capped luminescent bimetallic Au–Cu NCs having  $\lambda_{\text{em}}$  at 625 nm.<sup>241</sup> Briefly, an  $\text{HAuCl}_4$  solution was introduced in the PA solution under vigorous stirring. Subsequently,  $\text{Cu}(\text{NO}_3)_2$  dissolved in nitric acid solution was added to the reaction mixture under vigorous stirring. The color of the solution was changed from brown to milky white, showing the generation of PA–AuCu NCs. The pure product was obtained after centrifugation. They successfully demonstrated the enhancement in the emission intensity by varying either the amount of Cu or Au and keeping other parameters in the system fixed.

The restriction in intramolecular rotation through chemical bonds can also induce luminescence in bimetallic NPs having different oxidation states. The enhancement factor in bimetallic fluorescence dominates the fluorescence of the individual metallic system.<sup>242</sup> For example, reducing  $\text{Au}(\text{i})$  to  $\text{Au}(\text{0})$  by  $\text{NaBH}_4$  can induce a significant enhancement in fluorescence in the  $\text{Cu}^{\text{I}}\text{SR}^{\text{I}}$  ( $\text{R}^{\text{I}} = \text{C}_{10}\text{H}_{15}$ ) system in bimetallic  $\text{Au}_2\text{Cu}_6$  NCs, but it was observed that the same reaction without Au resulted in the absence of the emission band. The brief synthetic procedure for  $\text{Au}_2\text{Cu}_6$  involves the room-temperature reaction of  $\text{CuCl}$  in  $\text{CH}_3\text{CN}$  and  $\text{CH}_3\text{OH}$  and adamantanethiol in toluene under vigorous stirring. Then ice-cold  $[\text{Au}(\text{PPh}_2\text{Py})\text{Cl}]$  and

ice-cold water containing  $\text{NaBH}_4$  were introduced dropwise in the previous reaction mixture with vigorous stirring under an  $\text{N}_2$  atmosphere, and stirring was continued for 60 h. After the reaction, the pure product was obtained after centrifugation, washing and crystallization. The enhancement in the emission intensity was highly triggered by the restricted movement of the  $\text{Cu}^{\text{I}}\text{SR}$  system inside the crystal structure of  $\text{Au}_2\text{Cu}_6(\text{PPh}_2\text{Py})_2(\text{SC}_{10}\text{H}_{15})_6$ . A similar strategy was also extended to another system containing *t*-butyl mercaptan as the ligand system.<sup>243</sup> By modifying a previously reported procedure for introducing hetero-metallic atoms in the core of  $\text{Au}_{25}$  NCs,<sup>244</sup> Kazan *et al.* prepared emissive  $\text{Au}_{38}\text{Cu}_1(2\text{-PET})_{24}$ , (PET-2-phenylethanethiol) adduct nanoclusters by reacting as-prepared  $\text{Au}_{38}(2\text{-PET})_{24}$  in toluene with  $\text{Cu}(\text{i})\text{-}(\text{SR})$  at room temperature for 1 h followed by a few purification steps.<sup>153</sup> They successfully demonstrated the two-fold enhancement in the luminescence intensity by the introduction of  $\text{Cu}^{\text{I}}$  in the reaction system. Bazán-Díaz *et al.* synthesized 2D-nanoribbons comprised of Au/Cu NPs by controlling the assembly and growth of the metal precursors inside a soft template.<sup>152</sup> The flexible nanoribbons were synthesized by utilizing hexadecyl amine (HDA) as the surface protectant and self-assembly initiator. Dual-emitting nanoribbons were synthesized by reacting an aqueous solution of the metal precursors ( $\text{CuCl}_2$  and  $\text{HAuCl}_4$ ) with HDA in water under magnetic stirring at 60 °C until its color changed to mint green. Finally, an aqueous glucose solution was introduced in the reaction mixture.

The reaction was continued with another 30 min stirring, followed by centrifugation to get the desired product with narrow emission peaks at 700 and 813 nm. Nie *et al.* synthesized luminescent GSH–Cu/Au BMNCs at room temperature by reacting  $\text{Cu}(\text{NO}_3)_2$  solution with GSH solution.<sup>245</sup> The reaction proceeded *via* the formation of a white hydrogel. The dropwise addition of NaOH solution resulted in the formation of a transparent light-yellow solution at approximately pH 5. Finally, the reaction mixture containing CuNCs was added with aqueous  $\text{HAuCl}_4$  at room temperature with stirring. The desired products were obtained after a few rounds of purification. The GSH–Cu/Au BMNCs could be utilized as a potential candidate for chromium ion sensing and temperature sensing.

Bagheri and co-workers utilized the well-explored protein template BSA towards the synthesis of luminescent bimetallic Au–Cu NCs in aqueous medium.<sup>246</sup> This procedure involved the treatment of equimolar  $\text{HAuCl}_4$  and  $\text{Cu}(\text{NO}_3)_2$  with the BSA solution under constant stirring for 15 min, followed by the introduction of NaOH to maintain pH 12. After 12 h stirring, the pure product was obtained after dialysis. The Cu doping in the Au–BSA system enhanced the electrochemical catalytic properties *via* the synergistic effect. The authors investigated their properties towards determination of the bisphenol A.

Besides Ag and Cu, recently platinum has also been utilized for the doping of AuNCs. For example, in a typical hydrothermal synthesis, Wu and coworkers employed guanosine monophosphate (GMP) as the protecting ligand to synthesize luminescent Au–Pt bimetallic nanoclusters, which showed an emission band at 415 nm with  $\lambda_{\text{ex}} = 330$  nm (Fig. 26A and B).<sup>247</sup> One year later, the same group proposed another method for



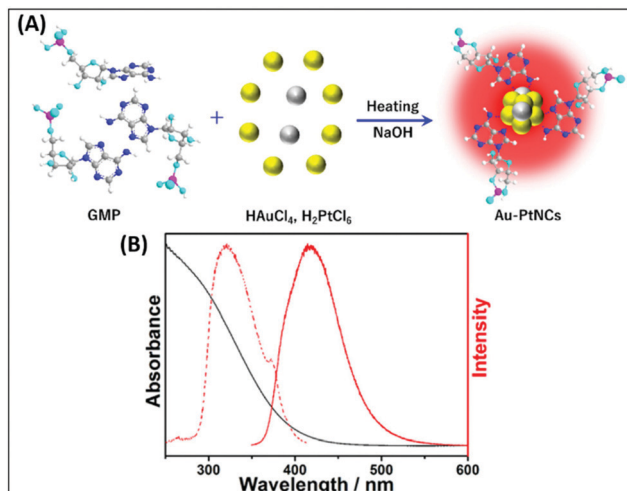


Fig. 26 (A) Schematic illustration of the synthetic procedure for Au-PtNCs-GMP and (B) excitation (red dotted line) and emission (red) spectra and UV-vis (black line) absorption spectrum of the Au-PtNCs-GMP BMNCs. Reproduced from ref. 247 with permission from the American Chemical Society, Copyright 2020.

the hydrothermal synthesis of GSH-stabilized Au-Pt BMNCs, which possessed both visible emission at 625 nm and NIR emission band at 805 nm, and finally utilized them towards the detection of Ag(i). An aqueous solution containing HAuCl<sub>4</sub> and K<sub>2</sub>PtCl<sub>4</sub> (8:1) was mixed with GSH and sodium citrate, and finally autoclaved with varying temperature and time to get pure BMNCs. When the reaction time was fixed to 1 h or 2 h, the corresponding BMNCs showed an emission band in the visible or NIR range.<sup>248</sup>

## 4. Summary and outlook

Luminescent AuNCs can emit from the blue to near-IR (NIR) spectral region depending on the number of atoms in the cluster. In recent years, various approaches have been developed to prepare highly photoluminescent AuNCs with emission in the UV-vis region, for example: (1) engineering the particle surface by using different ligands, DNA, peptides, and proteins including bovine serum albumin (BSA), (2) controlling the metal core size, (3) aggregation-induced emission and (4) rigidification of the Au(i)-thiolate shell.<sup>11,43,44,112,114,127,249,250</sup> Recent advances in the synthesis of AuNCs enabled the development of NIR-photoluminescent (NIR PL) AuNCs functionalized with a variety of thiol-containing ligands.<sup>251</sup>

These ligands exhibit a significant enhancement in the emission efficiency of AuNCs, *e.g.*, the optimized quantum yield (QY) of glutathione (GSH)-stabilized AuNCs reached about 15%, which can truly overcome the QY of less than 0.1% obtained from the classic Burst method for the synthesis of AuNCs.<sup>252</sup> The tunable emission of the protein-stabilized Au nanoclusters (AuNCs) over a large spectral range makes them a useful platform in biomedical studies. AuNCs can harness photon energy in the field of light harvesting materials by virtue of their discrete energy levels, which can extend the

lifetime of excited electrons up to the microsecond regime, which is 10<sup>6</sup> times larger than the ultrafast relaxation of hot electrons in the case of plasmonic nanoparticles.<sup>253</sup>

In general, the luminescence properties in these nanoclusters originate from the typical modulation of their HOMO-LUMO energy gap within discrete gold nanoclusters. These variations in energy gaps can also be introduced by incorporating another metal in the system. Bimetallic nanoclusters have been shown to possess better luminescence properties compared to their monometallic nanomaterials. The location of specific substituted metal atoms in the nanoclusters has a significant contribution in the enhancement of their luminescence properties. The synthetic aspects involving small molecules or biomolecules or their combinations as stabilizing agents in these metal-based nanomaterials were covered in this current review.

Scientists across the globe have recently focused on the applications of luminescent gold nanomaterials. The chemical and biological applications of these materials in analysis and sensing applications have drawn significant interest.<sup>216,254</sup> Increasing attempts have already been made to achieve AIE in highly luminescent metal nanocluster assemblies using hierarchical functional materials.<sup>127</sup> Luminescent gold nanomaterials have also been tested in devices and cellular imaging.<sup>255</sup>

Still, in comparison to the traditional highly promising emissive materials such as quantum dots (QDs) and organic dyes, most of the noble metal nanoclusters cannot show a higher fluorescence quantum yield although they are comparatively less toxic and safely renal-clearable. In some cases, aggregation-induced emission has demonstrated a promising enhancement in fluorescence from nanoclusters, but in this case, the limited hydrophilicity of the as-obtained products becomes an issue, which restricts their applications in living systems.<sup>64</sup> An improvement in the water solubility of these aggregation-induced emission based NCs can be done by encapsulating the aggregates with some additional water-soluble coating and engineering them with a controllable size to make them very impactful for future applications in therapeutics.

## Author contributions

K. B., J. K. S. and K. K. S. have contributed in all the topics.

## Conflicts of interest

There are no conflicts to declare.

## Acknowledgements

K. K. S. acknowledges DST Nanomission (DST/NM/NB/2018/237), SERB-DST Grants (EMR/2014/000714 and CRG/2018/000269) and CSIR Grant No. 01(2989)/19/EMR-II for funding to carry out research in this topic.



## Notes and references

- K. M. Dean and A. E. Palmer, *Nat. Chem. Biol.*, 2014, **10**, 512–523.
- E. Kim, Y. Lee, S. Lee and S. B. Park, *Acc. Chem. Res.*, 2015, **48**, 538–547.
- T. F. G. G. Cova, A. A. C. C. Pais and J. S. S. de Melo, *Sci. Rep.*, 2017, **7**, 6806.
- H. Kobayashi, M. Ogawa, R. Alford, P. L. Choyke and Y. Urano, *Chem. Rev.*, 2010, **110**, 2620–2640.
- K. K. Sadhu, S. Mizukami, Y. Hori and K. Kikuchi, *Chem. BioChem.*, 2011, **12**, 1299–1308.
- J. Zhang, X. Chai, X.-P. He, H.-J. Kim, J. Yoon and H. Tian, *Chem. Soc. Rev.*, 2019, **48**, 683–722.
- J. Tian, N. Cheng, Q. Liu, W. Xing and X. Sun, *Angew. Chem., Int. Ed.*, 2015, **54**, 5493–5497.
- A. N. Bismillah and I. Aprahamian, *Chem. Soc. Rev.*, 2021, **50**, 5631–5649.
- H. Xiao, W. Zhang, P. Li, W. Zhang, X. Wang and B. Tang, *Angew. Chem., Int. Ed.*, 2020, **59**, 4216–4230.
- L. Yuan, W. Lin, K. Zheng, L. He and W. Huang, *Chem. Soc. Rev.*, 2013, **42**, 622–661.
- S. Kolay, D. Bain, S. Maity, A. Devi, A. Patra and R. Antoine, *Nanomaterials*, 2022, **12**, 544.
- T. A. Tsunoyama, Y. Watanabe, J. Goto, K. Naito, R. S. Kasai, K. G. N. Suzuki, T. K. Fujiwara and A. Kusumi, *Nat. Chem. Biol.*, 2018, **14**, 497–506.
- L. Y. Mironov, P. S. Parfenov, A. V. Shurukhina, Y. I. Lebedev and A. A. Metlenko, *J. Phys. Chem. C*, 2017, **121**, 19958–19965.
- R. D. Mehlenbacher, R. Kolbl, A. Lay and J. A. Dionne, *Nat. Rev. Mater.*, 2018, **3**, 17080.
- X. Luo and J. Liu, *Adv. Sci.*, 2022, **9**, 2103971.
- Y. Zhou, F. Mazur, Q. Fan and R. Chandrawati, *View*, 2022, 20210008.
- C.-H. Chuang, W.-Y. Chen, W.-B. Tseng, A. Lin, C.-Y. Lu and W.-L. Tseng, *ACS Sustainable Chem. Eng.*, 2022, **10**, 2461–2472.
- D. Barman, K. Narang, R. Parui, N. Zehra, M. N. Khatun, L. R. Adil and P. K. Iyer, *Aggregate*, 2022, e172.
- C. Zhang, L. Yan, Z. Gu and Y. Zhao, *Chem. Sci.*, 2019, **10**, 6932–6943.
- W. Zhao, A. Li, A. Zhang, Y. Zheng and J. Liu, *ChemMed-Chem*, 2018, **13**, 2134–2149.
- C.-N. Lok, T. Zou, J.-J. Zhang, I. W.-S. Lin and C.-M. Che, *Adv. Mater.*, 2014, **26**, 5550–5557.
- C. F. Markwalter, A. G. Kantor, C. P. Moore, K. A. Richardson and D. W. Wright, *Chem. Rev.*, 2019, **119**, 1456–1518.
- B. Wang, W. Feng, Y. Zhao and Z. Chai, *Metallomics*, 2013, **5**, 793–803.
- Z. Xia and S. Guo, *Chem. Soc. Rev.*, 2019, **48**, 3265–3278.
- J. Yu, Y. Dai, Q. He, C. Cheng, Z. Shao and M. Ni, *Appl. Phys. Rev.*, 2020, **7**, 041304.
- J. Balach, J. Linnemann, T. Jaumann and L. Giebel, *J. Mater. Chem. A*, 2018, **6**, 23127–23168.
- V. C. Hoang, V. G. Gomes and N. Kornienko, *Nano Energy*, 2020, **78**, 105311.
- J. Mao, J. Li, J. Pei, Y. Lu, D. Wang and Y. Li, *Nano Today*, 2019, **26**, 164–175.
- L. Wang, W. Zheng, S. Li, L. Zhong and X. Jiang, *Nano Lett.*, 2022, **22**, 3576–3582.
- H. Huang, J. Zhao, B. Weng, F. Lai, M. Zhang, J. Hofkens, M. B. J. Roeffaers, J. A. Steele and J. Long, *Angew. Chem., Int. Ed.*, 2022, e202204563.
- C.-C. Chang, C.-F. Li, Z.-H. Yang, P.-Y. Lin, H.-C. Chang and C.-W. Yang, *Sens. Actuators, B*, 2022, **364**, 131823.
- Z. Tang, I. Surin, A. Rasmussen, F. Krumeich, E. V. Kondratenko, V. A. Kondratenko and J. Pérez-Ramírez, *Angew. Chem., Int. Ed.*, 2022, **61**, e20220077.
- Y. A. Hong and J. W. Ha, *Sci. Rep.*, 2022, **12**, 6983.
- L. Priest, J. S. Peters and P. Kukura, *Chem. Rev.*, 2021, **121**, 11937–11970.
- Y. Zhou, L. Liao, S. Zhuang, Y. Zhao, Z. Gan, W. Gu, J. Li, H. Deng, N. Xia and Z. Wu, *Angew. Chem., Int. Ed.*, 2021, **60**, 8668–8672.
- Q. Li, C. J. Zeman IV, Z. Ma, G. C. Schatz and X. W. Gu, *Small*, 2021, **17**, 2007992.
- G. Pramanik, K. Kvakova, M. A. Thottappalli, D. Rais, J. Pfleger, M. Greben, A. E. Zoka, S. Bals, M. Dracinsky, J. Valenta and P. Cigler, *Nanoscale*, 2021, **13**, 10462–10467.
- T. Kong, C. Zhang, X. Gan, F. Xiao, J. Li, Z. Fu, Z. Zhang and H. Zheng, *J. Mater. Chem. C*, 2020, **8**, 4338–4342.
- V. Kumar, P. Srikrishnarka, J. S. Mohanty, M. P. Kannan, R. Nagarajan and T. Pradeep, *ACS Sustainable Chem. Eng.*, 2021, **9**, 7431–7436.
- A. Chakraborty, H. Dave, B. Mondal, Nonappa, E. Khatun and T. Pradeep, *J. Phys. Chem. B*, 2022, **126**, 1842–1851.
- O. Pavelka, K. Kvakova, J. Vesely, J. Mizera, P. Cigler and J. Valenta, *Nanoscale*, 2022, **14**, 3166–3178.
- G. Wu, T. Jiang, W. Li, T. Liu and X. Ma, *Dyes Pigm.*, 2021, **188**, 109211.
- M. Wang, X. Zhou, X. Wang, M. Wang and X. Su, *Sens. Actuators, B*, 2021, **345**, 130407.
- M. Wactawska, H. Niegzanska and W. Dzwolak, *J. Mater. Chem. C*, 2022, **10**, 3775–3783.
- T. Zhang, C. Tang, Y. Wang, C. Wang, Y. Zhang, W. Qi, R. Su and Z. He, *Langmuir*, 2022, **38**, 4147–4155.
- M. Saini, S. Ghosh, V. Kumar, P. Roy and K. K. Sadhu, *Chem. – Eur. J.*, 2020, **26**, 15150–15158.
- K. Huang, Q. Fang, W. Sun, S. He, Q. Yao, J. Xie, W. Chen and H. Deng, *J. Phys. Chem. Lett.*, 2022, **13**, 419–426.
- B. Peng, L.-X. Zheng, P.-Y. Wang, J.-F. Zhou, M. Ding, H.-D. Sun, B.-Q. Shan and K. Zhang, *Front. Chem.*, 2021, **9**, 756993.
- S. Havenridge and C. M. Aikens, *J. Chem. Phys.*, 2021, **155**, 074302.
- Z. Wei, Y. Pan, G. Hou, X. Ran, Z. Chi, Y. He, Y. Kuang, X. Wang, R. Liu and L. Guo, *ACS Appl. Mater. Interfaces*, 2022, **14**, 2452–2463.
- A. Pniakowska and J. O. Banska, *Molecules*, 2022, **27**, 807.
- M. Wang, B. Duan, Y. Li, S. Jiang, Z. Huang and W. Yang, *ACS Appl. Nano Mater.*, 2021, **4**, 7486–7492.



53 D. Cheng, R. Liu, L. Tian, Q. Zhou, F. Niu, Y. Yue and K. Hu, *ACS Appl. Nano Mater.*, 2021, **4**, 13413–13424.

54 A. R. Ziefuss, T. Steenbock, D. Benner, A. Plech, J. Gotlicher, M. Teubner, B. Grimm-Lebsanft, C. Rehbock, C. C. Zerbino, R. Antoine, D. Amans, I. Chakraborty, G. Bester, M. Nachev, B. Sures, M. Rubhausen, W. J. Parak and S. Barcikowski, *Adv. Mater.*, 2021, **33**, 2101549.

55 J. Valenta, M. Greben, G. Pramanik, K. Kvakova and P. Cigler, *Phys. Chem. Chem. Phys.*, 2021, **23**, 11954–11960.

56 J. Liu, Y. Yu, C. Wang, J. Shen, J. Feng and W. Qi, *Chem. Commun.*, 2021, **57**, 10202–10205.

57 B. Casteleiro, J. M. G. Martinho and J. P. S. Farinha, *Nanoscale*, 2021, **13**, 17199–17217.

58 V. Hynninen, S. Chandra, S. Das, M. Amini, Y. Dai, S. Lepikko, P. Mohammadi, S. Hietala, R. H. A. Ras, Z. Sun, O. Ikkala and Nonappa, *Small*, 2021, **17**, 2005205.

59 S. M. Saleh, M. K. Almotiri and R. Ali, *J. Photochem. Photobiol. A*, 2022, **426**, 113719.

60 C. Kong, Y. Luo, W. Zhang, T. Lin, Z. Na, X. Liu and Z. Xie, *RSC Adv.*, 2022, **12**, 12060–12067.

61 J. Shen, Q. Xiao, P. Sun, J. Feng, X. Xin, Y. Yu and W. Qi, *ACS Nano*, 2021, **15**, 4947–4955.

62 L. Li, T. Yang, J. Yang and X. Zhang, *Sens. Actuators, B*, 2022, **353**, 131038.

63 H. Chen, Y. Chang, R. Wei and P. Zhang, *Anal. Methods*, 2022, **14**, 1439–1444.

64 S. Li, Q. Ma, C. Wang, K. Yang, Z. Hong, Q. Chen, J. Song, X. Song and H. Yang, *Anal. Chem.*, 2022, **94**, 2641–2647.

65 S. Dolui, S. Basu and A. Paul, *Mater. Adv.*, 2022, **3**, 3286–3292.

66 Y. Pan, X. Wei, X. Guo, H. Wang, H. Song, C. Pan and N. Xu, *Biosens. Bioelectron.*, 2021, **194**, 113611.

67 B. Fu, X. Zheng, H. Li, L. Ding, F. Wang, D.-Y. Guo, W. Yang and Q. Pan, *Sens. Actuators, B*, 2021, **346**, 130502.

68 M. Wang, X. Zhou, L. Cheng, M. Wang and X. Su, *ACS Appl. Nano Mater.*, 2021, **4**, 9265–9273.

69 Z. Zhou, T. Shu, Y. Sun, H. Si, P. Peng, L. Su and X. Zhang, *Biosens. Bioelectron.*, 2021, **192**, 113530.

70 Y. Sun, T. Shu, J. Ma, Q. Dai, P. Peng, Z. Zhou, X. Zhou, L. Su and X. Zhang, *Anal. Chem.*, 2022, **94**, 3408–3417.

71 Y. Tao, K. Yi, H. Wang, K. Li and M. Li, *Sens. Actuators, B*, 2022, **361**, 131711.

72 M. Xie, Y. Wang, L. Liu, X. Wang and H. Jiang, *J. Colloid Interface Sci.*, 2022, **614**, 502–510.

73 Y. Cong, X. Wang, S. Zhu, L. Liu and L. Li, *ACS Appl. Bio Mater.*, 2021, **4**, 2790–2797.

74 Z. Li, H. Peng, J. Liu, Y. Tian, W. Yang, J. Yao, Z. Shao and X. Chen, *ACS Appl. Mater. Interfaces*, 2018, **10**, 83–90.

75 F. Yu, Z. Cao, S. He, H. Xiang, G. Zhao, L. Yang and H. Liu, *Chem. Commun.*, 2022, **58**, 811–814.

76 Y.-F. Kang, B. Zheng, C.-Y. Li, Z.-L. Zhang, H.-W. Tang, Q.-S. Wu and D.-W. Pang, *Anal. Chem.*, 2020, **92**, 1292–1300.

77 S. Zhai, W. Hu, C. Fan, W. Feng and Z. Liu, *Chem. Commun.*, 2021, **57**, 5542–5545.

78 Y.-T. Yen, Y.-J. Chang, Y.-T. Tseng, C.-Y. Chen, Y.-L. Liu and H.-T. Chang, *Sens. Actuators, B*, 2022, **353**, 131151.

79 J. Liang, H. Xiong, W. Wang, W. Wen, X. Zhang and S. Wang, *Sens. Actuators, B*, 2018, **255**, 2170–2178.

80 H. Zhu, N. Liu, Z. Wang, Q. Xue, Q. Wang, X. Wang, Y. Liu, Z. Yin and X. Yuan, *Nanoscale*, 2021, **13**, 18996–19003.

81 J. Yang, Y. Peng, S. Li, J. Mu, Z. Huang, J. Ma, Z. Shi and Q. Jia, *Coord. Chem. Rev.*, 2022, **456**, 214391.

82 I. M. Khan, S. Niazi, L. Yue, Y. Zhang, I. Pasha, M. K. I. Khan, W. Akhtar, A. Mohsin, M. F. J. Chughati and Z. Wang, *Talanta*, 2022, **241**, 123228.

83 S. Qian, Z. Wang, Z. Zuo, X. Wang, Q. Wang and X. Yuan, *Coord. Chem. Rev.*, 2022, **451**, 214268.

84 H. Shen, C. Xu, F. Sun, M. Zhao, Q. Wu, J. Zhang, S. Li, J. Zhang, J. W. Y. Lam and B. Z. Tang, *ChemMedChem*, 2022, **17**, e202100578.

85 M.-M. Zhang, X.-Y. Dong, Y.-J. Wang, S.-Q. Zang and T. C. W. Mak, *Coord. Chem. Rev.*, 2022, **453**, 214315.

86 Y. Xiao, Z. Wu, Q. Yao and J. Xie, *Aggregate*, 2021, **2**, 114–132.

87 S. Bothra and S. K. Sahoo, *Sensing and Biosensing with Optically Active Nanomaterials*, ed. S. K. Sahoo, *Elsevier*, 1st edn, 2022, pp. 207–242.

88 L. Zhao, Y. Zhou, G. Niu, F. Gao, Z. Sun, H. Li and Y. Jiang, *Part. Part. Syst. Charact.*, 2022, 2100231.

89 S. Zhan, J. Jiang, Z. Zeng, Y. Wang and H. Cui, *Coord. Chem. Rev.*, 2022, **455**, 214381.

90 M. T. Nguyen, L. Deng and T. Yonezawa, *Soft Matter*, 2022, **18**, 19–47.

91 D. Ungor, Á. Juhász, N. Varga and E. Csapó, *Adv. Colloid Interface Sci.*, 2022, **301**, 102616.

92 A. González-Rosell, C. Cerretani, P. Mastracco, T. Vosch and S. M. Copp, *Nanoscale Adv.*, 2021, **3**, 1230–1260.

93 I. Zare, D. M. Chevrier, A. Cifuentes-Rius, N. Moradi, Y. Xianyu, S. Ghosh, L. Trapiella-Alfonso, Y. Tian, A. Shourangiz-Haghghi, S. Mukherjee, K. Fan and M. R. Hamblin, *Mater. Today*, 2021, DOI: [10.1016/j.mattod.2020.10.027](https://doi.org/10.1016/j.mattod.2020.10.027).

94 M. Sharifi, S. H. Hosseinali, R. H. Alizadeh, A. Hasan, F. Attar, A. Salihi, M. S. Shekha, K. M. Amen, F. M. Aziz, A. A. Saboury, K. Akhtari, A. Taghizadeh, N. Hooshmand, M. A. El-Sayed and M. Falahati, *Talanta*, 2020, **212**, 120782.

95 L. Wang, M. H. Kafshgari and M. Meunier, *Adv. Funct. Mater.*, 2020, **30**, 2005400.

96 N. Sarfraz and I. Khan, *Chem. – Asian J.*, 2021, **16**, 720–742.

97 H. Cui, Z.-S. Shao, Z. Song, Y.-B. Wang and H.-S. Wang, *J. Mater. Chem. C*, 2020, **8**, 14312–14333.

98 T.-Q. Yang, B. Peng, B.-Q. Shan, Y.-X. Zong, J.-G. Jiang, P. Wu and K. Zhang, *Nanomaterials*, 2020, **10**, 261.

99 M. Z. Iqbal, I. Ali, W. S. Khan, X. Kong and E. Dempsey, *Mater. Des.*, 2021, **205**, 109694.

100 A. Mooradian, *Phys. Rev. Lett.*, 1969, **22**, 185–187.

101 Y. Xiao, Z. Wu, Q. Yao and J. Xie, *Aggregate*, 2021, **2**, 114–132.

102 S. Link, A. Beeby, S. FitzGerald, M. A. El-Sayed, T. G. Schaaff and R. L. Whetten, *J. Phys. Chem. B*, 2002, **106**, 3410–3415.

103 E. S. Shibu, M. A. H. Muhammed, T. Tsukuda and T. Pradeep, *J. Phys. Chem. C*, 2008, **112**, 12168–12176.



104 Z. Wu and R. Jin, *Nano Lett.*, 2010, **10**, 2568–2573.

105 N. Goswami, Q. Yao, Z. Luo, J. Li, T. Chen and J. Xie, *J. Phys. Chem. Lett.*, 2016, **7**, 962–975.

106 R. Antoine and V. Bonačić-Koutecký, *Liganded silver and gold quantum clusters. Towards a new class of nonlinear optical nanomaterials*, Springer Nature, Cham, Switzerland, 2018, pp. 11–12.

107 G. Wang, T. Huang, R. W. Murray, L. Menard and R. G. Nuzzo, *J. Am. Chem. Soc.*, 2005, **127**, 812–813.

108 G. Wang, R. Guo, G. Kalyuzhny, J.-P. Choi and R. W. Murray, *J. Phys. Chem. B*, 2006, **110**, 20282–20289.

109 P. Londoño-Larrea, J. P. Vanegas, D. Cuaran-Acosta, E. Zaballos-García and J. Pérez-Prieto, *Chem. – Eur. J.*, 2017, **23**, 8137–8141.

110 K. L. Dimuthu, M. Weerawardene and C. M. Aikens, *J. Am. Chem. Soc.*, 2016, **138**, 11202–11210.

111 M. Zhou and Y. Song, *J. Phys. Chem. Lett.*, 2021, **12**, 1514–1519.

112 D. Chen and J. Li, *Nanoscale Horiz.*, 2020, **5**, 1355–1367.

113 L. Zhu, Y. Zeng, M. Teubner, B. Grimm-Lebsanft, A. R. Ziefuß, C. Rehbock, M. A. Rübhausen, S. Barcikowski, W. J. Parak and I. Chakraborty, *ACS Appl. Nano Mater.*, 2021, **4**, 3197–3203.

114 S. Kundu, B. Ghosh, S. Nandi, M. Ghosh, A. Pyne, J. Chatterjee and N. Sarkar, *ACS Appl. Bio Mater.*, 2020, **3**, 4282–4293.

115 J.-U. Kim, S.-H. Cha, K. Shin, J. Y. Jho and J.-C. Lee, *J. Am. Chem. Soc.*, 2005, **127**, 9962–9963.

116 Z. Luo, X. Yuan, Y. Yu, Q. Zhang, D. T. Leong, J. Y. Lee and J. Xie, *J. Am. Chem. Soc.*, 2012, **134**, 16662–16670.

117 N. Goswami, F. Lin, Y. Liu, D. T. Leong and J. Xie, *Chem. Mater.*, 2016, **28**, 4009–4016.

118 H. Chang, N. S. Karan, K. Shin, M. S. Bootharaju, S. Nah, S. I. Chae, W. Baek, S. Lee, J. Kim, Y. J. Son, T. Kang, G. Ko, S.-H. Kwon and T. Hyeon, *J. Am. Chem. Soc.*, 2021, **143**, 326–334.

119 A. J. Moro, J. Avó, M. Malfois, F. Zaccaria, C. F. Guerra, F. J. Caparrós, L. Rodríguez and J. C. Lima, *Dalton Trans.*, 2020, **49**, 171–178.

120 W. Sun, L. Luo, Y. Feng, Y. Cai, Y. Zhuang, R.-J. Xie, X. Chen and H. Chen, *Angew. Chem., Int. Ed.*, 2020, **59**, 9914–9921.

121 Y. Hua, Y. Wang, X. Kang, F. Xu, Z. Han, C. Zhang, Z.-Y. Wang, J.-Q. Liu, X. Zhao, X. Chen and S.-Q. Zang, *J. Nanobiotechnol.*, 2021, **19**, 1–14.

122 H. Zou, J. Zhang, C. Wu, B. He, Y. Hu, H. H. Y. Sung, R. T. K. Kwok, J. W. Y. Lam, L. Zheng and B. Z. Tang, *ACS Nano*, 2021, **15**, 9176–9185.

123 T. Pan, T. Zhou, Y. Tu and J. Yan, *Talanta*, 2021, **227**, 122197.

124 Y. Zi, D. Xu, C. Li, F. Qu and X.-E. Zhao, *Sens. Actuators, B*, 2021, **345**, 130243.

125 Y. Li, S. Teng, M. Wang, B. Duan and Z. Huang, *Sens. Actuators, B*, 2021, **330**, 129290.

126 J. M. Carnerero, A. Jimenez-Ruiz, P. M. Castillo and R. Prado-Gotor, *ChemPhysChem*, 2017, **18**, 17–33.

127 D. Bera and N. Goswami, *J. Phys. Chem. Lett.*, 2021, **12**, 9033–9046.

128 C. Zhou, C. Sun, M. Yu, Y. Qin, J. Wang, M. Kim and J. Zheng, *J. Phys. Chem. C*, 2010, **114**, 7727–7732.

129 L. Li, Z. Li, H. Zhang, S. Zhang, I. Majeed and B. Tan, *Nanoscale*, 2013, **5**, 1986–1992.

130 S. Palmal, S. Basiruddin, A. R. Maity, S. C. Ray and N. R. Jana, *Chem. – Eur. J.*, 2013, **19**, 943–949.

131 X. Wen, P. Yu, Y.-R. Toh, A.-C. Hsu, Y.-C. Lee and J. Tang, *J. Phys. Chem. C*, 2012, **116**, 19032–19038.

132 J. K. Sahu, S. A. Lone and K. K. Sadhu, *Langmuir*, 2022, **38**, 5865–5873.

133 D. Bain, S. Maity and A. Patra, *Chem. Commun.*, 2020, **56**, 9292–9295.

134 S. Chakraborty, D. Bain, S. Maity, S. Kolay and A. Patra, *J. Phys. Chem. C*, 2022, **126**, 2896–2904.

135 S. Wang, X. Meng, A. Das, T. Li, Y. Song, T. Cao, X. Zhu, M. Zhu and R. Jin, *Angew. Chem., Int. Ed.*, 2014, **53**, 2376–2380.

136 K. Nobusada and T. Iwasa, *J. Phys. Chem. C*, 2007, **111**, 14279–14282.

137 M. Y. Sfeir, H. Qian, K. Nobusada and R. Jin, *J. Phys. Chem. C*, 2011, **115**, 6200–6207.

138 G. Soldan, M. A. Aljuhani, M. S. Bootharaju, L. G. AbdulHalim, M. R. Parida, A. Emwas, O. F. Mohammed and O. M. Bakr, *Angew. Chem., Int. Ed.*, 2016, **55**, 5749–5753.

139 X.-Y. Xie, P. Xiao, X. Cao, W.-H. Fang, G. Cui and M. Dolg, *Angew. Chem., Int. Ed.*, 2018, **57**, 9965–9969.

140 R. Galassi, M. M. Ghimire, B. M. Otten, S. Riccia, R. N. M. Jr, R. M. Almotawa, D. Alhmoud, J. F. Ivy, A.-M. M. Rawashdeh, V. N. Nesterov, E. W. Reinheimer, L. M. Daniels, A. Burinia and M. A. Omary, *Proc. Natl. Acad. Sci. U. S. A.*, 2017, **114**, E5042–E5051.

141 D. Wang, R. Cai, S. Sharma, J. Jirak, S. K. Thummanapelli, N. G. Akhmedov, H. Zhang, X. Liu, J. L. Petersen and X. Shi, *J. Am. Chem. Soc.*, 2012, **134**, 9012–9019.

142 J. S. Mohanty, P. L. Xavier, K. Chaudhari, M. S. Bootharaju, N. Goswami, S. K. Pal and T. Pradeep, *Nanoscale*, 2012, **4**, 4255–4262.

143 N. Zhang, Y. Si, Z. Sun, L. Chen, R. Li, Y. Qiao and H. Wang, *Anal. Chem.*, 2014, **86**, 11714–11721.

144 B. Zhenga, J. Zhenga, T. Yua, A. Sanga, J. Dua, Y. Guoa, D. Xiaoa and M. M. F. Choi, *Sens. Actuators, B*, 2015, **221**, 386–392.

145 Q. Yuan, X. Kang, D. Hu, C. Qin, S. Wang and M. Zhu, *Dalton Trans.*, 2019, **48**, 13190–13196.

146 S. Basu, M. P. Bakulic, H. Fakhouri, I. Russier-Antoine, C. Moulin, P.-F. Brevet, V. Bonac-Koutecký and R. Antoine, *J. Phys. Chem. C*, 2020, **124**, 19368–19374.

147 X. Hu, Y. Zhang, T. Ding, J. Liu and H. Zhao, *Front. Bioeng. Biotechnol.*, 2020, **8**, 990.

148 Y. Li, T. Zhai, J. Chen, J. Shi, L. Wang, J. Shen and X. Liu, *Chem. – Eur. J.*, 2022, **28**, e202103736.

149 H. Tada, *Dalton Trans.*, 2022, **51**, 3383–3393.

150 I. Zare, M. T. Yaraki, G. Speranza, A. H. Najafabadi, A. Shourangiz-Haghghi, A. B. Nik, B. B. Manshian,



C. Saraiva, S. J. Soenen, M. J. Kogan, J. W. Lee, N. V. Apollo, L. Bernardino, E. Araya, D. Mayer, G. Mao and M. R. Hamblin, *Chem. Soc. Rev.*, 2022, **51**, 2601–2680.

151 R. Petrucci, M. Bortolami, P. D. Matteo and A. Curulli, *Nanomaterials*, 2022, **12**, 959.

152 P. Yuan, R. Ma, N. Gao, M. Garai and Q.-H. Xu, *Nanoscale*, 2015, **7**, 10233–10239.

153 R. Kazan, B. Zhang and T. Bürgi, *Dalton Trans.*, 2017, **46**, 7708–7713.

154 L. Bazán-Díaz, R. Mendoza-Cruz, J. J. Velázquez-Salazar, G. Plascencia-Villa, F. M. Ascencio-Aguirre, H. J. Ojeda-Galván, R. Herrera-Becerra, G. Guisbiers and M. José-Yacamán, *Langmuir*, 2018, **34**, 9394–9401.

155 Z. Chen, W. Ding, Y. Gu, S. Gao, D. Yun, C. Wang, W. Li and F. Sun, *Langmuir*, 2020, **36**, 13928–13936.

156 S. Li, W. Tian and Y. Liu, *Nanoscale*, 2021, **13**, 16847–16859.

157 Y. Li, M. Zhou and R. Jin, *Adv. Mater.*, 2021, **33**, 2006591.

158 A. Cantelli, G. Guidetti, J. Manzi, V. Caponetti and M. Montalti, *Eur. J. Inorg. Chem.*, 2017, 5068–5084.

159 J. Xie, Y. Zheng and J. Y. Ying, *J. Am. Chem. Soc.*, 2009, **131**, 888–889.

160 X. Y. Wong, D. Quesada-González, S. Manickam, S. Y. New, K. Muthooosamy and A. Merkoçi, *Sci. Rep.*, 2021, **11**, 2375.

161 Q. Li, R. Zhou, Y. Sun, D. Xiao, M. Liu, D. Zhao, S. Peng, Y. Chen and Y. Lin, *ACS Appl. Mater. Interfaces*, 2021, **13**, 11708–11720.

162 V. Jain, S. Bhagat and S. Singh, *Sens. Actuators, B*, 2021, **327**, 128886.

163 L. Zhang, M. Zhang and Y. Wu, *J. Mol. Struct.*, 2014, **1069**, 245–250.

164 A.-M. Hada, A.-M. Craciun, M. Focsan, R. Borlan, O. Soritau, M. Todea and S. Astilean, *Talanta*, 2021, **225**, 121960.

165 D. Ungor, A. Barbasz, A. Czyzowska, E. Csapó and M. Ocwieja, *Colloids Surf., B*, 2021, **200**, 111593.

166 J. Li, C. Xiao, W. Wei, R. Xiao, H. Yao and H. Liu, *ACS Appl. Mater. Interfaces*, 2021, **13**, 36632–36643.

167 Y. Niu, T. Ding, J. Liu, G. Zhang, L. Tong, X. Cheng, Y. Yang, Z. Chen and B. Tang, *Talanta*, 2021, **223**, 121745.

168 S. Chakraborty, A. Nandy, S. Ghosh, N. K. Das, S. Parveen, S. Datta and S. Mukherjee, *Analyst*, 2021, **146**, 1455–1463.

169 L. Yan, Y. Cai, B. Zheng, H. Yuan, Y. Guo, D. Xiao and M. M. F. Choi, *J. Mater. Chem.*, 2012, **22**, 1000–1005.

170 Y. Tao, K. Yi, H. Hu, D. Shao and M. Li, *J. Mater. Chem. B*, 2021, **9**, 94–100.

171 Y. Zhang, H. Jiang and X. Wang, *Anal. Chim. Acta*, 2015, **870**, 1–7.

172 P. S. Devi, S. Banerjee, S. R. Chowdhury and G. S. Kumar, *RSC Adv.*, 2012, **2**, 11578–11585.

173 Y. Yu, Z. Luo, Y. Yu, J. Y. Lee and J. Xie, *ACS Nano*, 2012, **6**, 7920–7927.

174 E. R. Gran, F. Bertorelle, H. Fakhouri, R. Antoine, M. P. Bakulić, Ž. S. Maršić, V. Bonačić-Koutecký, M. Blain, J. Antel and D. Maysinger, *Nanoscale*, 2021, **13**, 3173–3183.

175 L. Yang, B. Zhang, L. Fu, K. Fu and G. Zou, *Angew. Chem., Int. Ed.*, 2019, **58**, 6901–6905.

176 H. Liu, G. Hong, Z. Luo, J. Chen, J. Chang, M. Gong, H. He, J. Yang, X. Yuan, L. Li, X. Mu, J. Wang, W. Mi, J. Luo, J. Xie and X.-D. Zhang, *Adv. Mater.*, 2019, **31**, 1901015.

177 T. Pan, T. Zhou, Y. Tu and J. Yan, *Talanta*, 2021, **227**, 122197.

178 F. Bertorelle, I. Russier-Antoine, N. Calin, C. Comby-Zerbino, A. Bensalah-Ledoux, S. Guy, P. Dugourd, P.-F. Brevet, Ž. Sanader, M. Krstić, V. Bonačić-Koutecký and R. Antoine, *J. Phys. Chem. Lett.*, 2017, **8**, 1979–1985.

179 I. Russier-Antoine, F. Bertorelle, M. Vojkovic, D. Rayane, E. Salmon, C. Jonin, P. Dugourd, R. Antoine and P.-F. Brevet, *Nanoscale*, 2014, **6**, 13572–13578.

180 F. Bertorelle, C. Moulin, A. Soleilhac, C. Comby-Zerbino, P. Dugourd, I. Russier-Antoine, P.-F. Brevet and R. Antoine, *ChemPhysChem*, 2018, **19**, 165–168.

181 P. Huang, S. Li, N. Gao and F. Wu, *Analyst*, 2015, **140**, 7313–7321.

182 V. Venkatesh, A. Shukla, S. Sivakumar and S. Verma, *ACS Appl. Mater. Interfaces*, 2014, **6**, 2185–2191.

183 C.-C. Huang, Z. Yang, K.-H. Lee and H.-T. Chang, *Angew. Chem., Int. Ed.*, 2007, **46**, 6824–6828.

184 J. Sun, J. Zhang and Y. Jin, *J. Mater. Chem. C*, 2013, **1**, 138–143.

185 F. Aldeek, M. A. H. Muhammed, G. Palui, N. Zhan and H. MattoSSI, *ACS Nano*, 2013, **7**, 2509–2521.

186 Y. Li, S. Yi, Z. Lei and Y. Xiao, *RSC Adv.*, 2021, **11**, 14678–14685.

187 Z. Lei, J.-J. Li, Z.-A. Nan, Z.-G. Jiang and Q.-M. Wang, *Angew. Chem., Int. Ed.*, 2021, **60**, 14415–14419.

188 J. Wang, Z.-Y. Wang, S.-J. Li, S.-Q. Zang and T. C. W. Mak, *Angew. Chem., Int. Ed.*, 2021, **60**, 5959–5964.

189 X.-K. Wan, W. W. Xu, S.-F. Yuan, Y. Gao, X.-C. Zeng and Q.-M. Wang, *Angew. Chem., Int. Ed.*, 2015, **54**, 9683–9686.

190 X.-S. Han, X. Luan, H.-F. Su, J.-J. Li, S.-F. Yuan, Z. Lei, Y. Pei and Q.-M. Wang, *Angew. Chem., Int. Ed.*, 2020, **59**, 2309–2312.

191 K. Pyo, N. H. Ly, S. Y. Yoon, Y. Shen, S. Y. Choi, S. Y. Lee, S.-W. Joo and D. Lee, *Adv. Healthcare Mater.*, 2017, **6**, 1700203.

192 L. Kacenauskaite, N. Bisballe, R. Mucci, M. Santella, T. Pullerits, J. Chen, T. Vosch and B. W. Laursen, *J. Am. Chem. Soc.*, 2021, **143**, 1377–1385.

193 D. J. Lewis, T. M. Day, J. V. MacPherson and Z. Pikramenou, *Chem. Commun.*, 2006, 1433–1435.

194 C.-Z. Li, K. B. Male, S. Hrapovic and J. H. T. Luong, *Chem. Commun.*, 2005, 3924–3926.

195 H. He, C. Xie and J. Ren, *Anal. Chem.*, 2008, **80**, 5951–5957.

196 G. F. Walsh and L. D. Negro, *Nano Lett.*, 2013, **13**, 786–792.

197 M. Saini, Y. Masirkar, R. Varshney, P. Roy and K. K. Sadhu, *Chem. Commun.*, 2017, **53**, 6199–6202.

198 M. Saini, A. Verma, K. Tomar, P. K. Bharadwaj and K. K. Sadhu, *Chem. Commun.*, 2018, **54**, 12836–12839.

199 K. Bharti, S. A. Lone, A. Singh, S. Nathani, P. Roy and K. K. Sadhu, *Front. Chem.*, 2021, **9**, 639090.

200 I. Chakraborty and T. Pradeep, *Chem. Rev.*, 2017, **117**, 8208–8271.

201 X. Yuan, X. Dou, K. Zheng and J. Xie, *Part. Part. Syst. Charact.*, 2015, **32**, 613–629.



202 M. Linden, A. J. Bunningen, L. Amidani, M. Bransen, H. Elnaggar, P. Glatzel, A. Meijerink and F. M. F. Groot, *ACS Nano*, 2018, **12**, 12751–12760.

203 A. Sannigrahi, S. Chowdhury, I. Nandi, D. Sanyal, S. Chall and K. Chattopadhyay, *Nanoscale Adv.*, 2019, **1**, 3660–3669.

204 X. Qu, Y. Li, L. Li, Y. Wang, J. Liang and J. Liang, *J. Nanomater.*, 2015, **2015**, 1–23.

205 S. L. Fereja, P. Li, J. Guo, Z. Fang, Z. Zhang, Z. Zhuang, X. Zhang, K. Liu and W. Chen, *Talanta*, 2021, **233**, 122469.

206 Q. Li, L. Li, L. Chen, C. Wang, C. Li, K. Li and Y. Lin, *J. Nanosci. Nanotechnol.*, 2020, **20**, 692–700.

207 R. Dai, W. Deng, P. Hu, C. You, L. Yang, X. Jiang, X. Xiong and K. Huang, *Microchem. J.*, 2018, **139**, 1–8.

208 B. Zheng, J. Zheng, T. Yu, A. Sang, J. Du, Y. Guo, D. Xiao and M. M. F. Choi, *Sens. Actuators, B*, 2015, **221**, 386–392.

209 H. Huang, H. Li, J.-J. Feng and A.-J. Wang, *Sens. Actuators, B*, 2016, **223**, 550–556.

210 D. Hikosou, S. Saita, S. Miyata, H. Miyaji, T. Furuike, H. Tamura and H. Kawasaki, *J. Phys. Chem. C*, 2018, **122**, 12494–12501.

211 K. Brach, M. Waszkiewicz, J. Olesiak-Banska, M. Samoc and K. Matczyszyn, *Langmuir*, 2017, **33**, 8993–8999.

212 T. Ye and X. An, *New J. Chem.*, 2019, **43**, 569–572.

213 M. Liu, N. Li, Y. He, Y. Ge and G. Song, *Microchim. Acta*, 2018, **185**, 147.

214 Z. Yin, Z. Wang, X. Dai, N. Liu, S. Wang, G. Li, F. Du and X. Yuan, *ACS Sustainable Chem. Eng.*, 2020, **8**, 15336–15343.

215 R. Kobayashi, Y. Nonoguchi, A. Sasaki and H. Yao, *J. Phys. Chem. C*, 2014, **118**, 15506–15515.

216 T. Udayabhaskararao, Y. Sun, N. Goswami, S. K. Pal, K. Balasubramanian and T. Pradeep, *Angew. Chem., Int. Ed.*, 2012, **51**, 2155–2159.

217 J. Sun, H. Wuab and Y. Jin, *Nanoscale*, 2014, **6**, 5449–5457.

218 Y. Yang, Y. Sun, S. Liao, Z. Wu and R. Yu, *Anal. Methods*, 2016, **8**, 7237–7241.

219 S. Ristig, D. Kozlova, W. Meyer-Zaika and M. Epple, *J. Mater. Chem. B*, 2014, **2**, 7887–7895.

220 R. D. Corpuz, Y. Ishida, M. T. Nguyen and T. Yonezawa, *Langmuir*, 2017, **33**, 9144–9150.

221 F. Yu, P. Luo, Y. Chen, H. Jiang and X. Wang, *Anal. Methods*, 2021, **13**, 2575–2585.

222 Q. Liu, X. Yan, Q. Lai and X. Su, *Sens. Actuators, B*, 2019, **282**, 45–51.

223 W.-Y. Chen, G.-Y. Lan and H.-T. Chang, *Anal. Chem.*, 2011, **83**, 9450–9455.

224 S. Liu and S. Pang, *Microchim. Acta*, 2018, **185**, 426.

225 T. Li, H. Yi, Y. Liu, Z. Wang, S. Liu, N. He, H. Liu and Y. Deng, *J. Biomed. Nanotechnol.*, 2018, **14**, 150–160.

226 Y. Zhang, H. Jiang, W. Ge, Q. Li and X. Wang, *Langmuir*, 2014, **30**, 10910–10917.

227 J. Liu, X.-X. Yuan, H.-W. Li and Y. Wu, *J. Mater. Chem. C*, 2017, **5**, 9979–9985.

228 Z. Suo, X. Hou, J. Chen, X. Liu, Y. Liu, F. Xing, Y. Chen and L. Feng, *J. Phys. Chem. C*, 2020, **124**, 21094–21102.

229 S. Pang and S. Liu, *Anal. Methods*, 2017, **9**, 6713–6718.

230 F. Meng, F. Gan and G. Ye, *Microchim. Acta*, 2019, **186**, 371.

231 L. Fu, X. Gao, S. Dong, H.-Y. Hsu and G. Zou, *Anal. Chem.*, 2021, **93**, 4909–4915.

232 L. Tian, Y. Li, T. Ren, Y. Tong, B. Yang and Y. Li, *Talanta*, 2017, **170**, 530–539.

233 S. Pramanik, A. Saha and P. Sujatha Devi, *RSC Adv.*, 2015, **5**, 33946–33954.

234 W. Wu, T. Zhou and S. Zhou, *Chem. Mater.*, 2009, **21**, 2851–2861.

235 R. Contreras-Caceres, P. Alonso-Cristobal, D. Mendez-Gonzalez, M. Laurenti, A. Maldonado-Valdivia, F. Garcia-Blanco, E. L. Cabarcos, A. Fernandez-Barbero, J. Lopez-Romero and J. Rubio-Retama, *Langmuir*, 2014, **30**, 15560–15567.

236 L. G. AbdulHalim, M. S. Bootharaju, Q. Tang, S. D. Gobbo, R. G. AbdulHalim, M. Eddaoudi, D. Jiang and O. M. Bakr, *J. Am. Chem. Soc.*, 2015, **137**, 11970–11975.

237 M. S. Bootharaju, C. P. Joshi, M. R. Parida, O. F. Mohammed and O. M. Bakr, *Angew. Chem., Int. Ed.*, 2016, **55**, 922–926.

238 C. P. Joshi, M. S. Bootharaju, M. J. Alhilaly and O. M. Bakr, *J. Am. Chem. Soc.*, 2015, **137**, 11578–11581.

239 M. Linden, A. Barendregt, A. J. Bunningen, P. T. K. Chin, D. Thies-Weesie, F. M. F. Groot and A. Meijerink, *Nanoscale*, 2016, **8**, 19901–19909.

240 C. M. Andolina, A. C. Dewar, A. M. Smith, L. E. Marbella, M. J. Hartmann and J. E. Millstone, *J. Am. Chem. Soc.*, 2013, **135**, 5266–5269.

241 P.-C. Chen, J.-Y. Ma, L.-Y. Chen, G.-L. Lin, C.-C. Shih, T.-Y. Lin and H.-T. Chang, *Nanoscale*, 2014, **6**, 3503–3507.

242 S. Sculfort and P. Braunstein, *Chem. Soc. Rev.*, 2011, **40**, 2741–2760.

243 X. Kang, S. Wang, Y. Song, S. Jin, G. Sun, H. Yu and M. Zhu, *Angew. Chem., Int. Ed.*, 2016, **55**, 3611–3614.

244 S. Wang, Y. Song, S. Jin, X. Liu, J. Zhang, Y. Pei, X. Meng, M. Chen, P. Li and M. Zhu, *J. Am. Chem. Soc.*, 2015, **137**, 4018–4021.

245 F. Nie, L. Ga, J. Ai and Y. Wang, *RSC Adv.*, 2018, **8**, 13708–13713.

246 E. Mahmoudi, A. Hajian, M. Rezaei, A. Afkhami, A. Amine and H. Bagheri, *Microchem. J.*, 2019, **145**, 242–251.

247 C.-X. Zhang, Y.-C. Gao, H.-W. Li and Y. Wu, *ACS Appl. Nano Mater.*, 2020, **3**, 9318–9328.

248 Y.-C. Gao, C. Wang, C.-X. Zhang, H.-W. Li and Y. Wu, *Microchim. Acta*, 2021, **188**, 50.

249 V. G. Deepagan, M. N. Leiske, N. L. Fletcher, D. Rudd, T. Tieu, N. Kirkwood, K. J. Thurecht, K. Kempe, N. H. Voelcker and A. Cifuentes-Rius, *Nano Lett.*, 2021, **21**, 476–484.

250 X.-Y. Wang, J. Zhang, J. Yin, S. H. Liu and B. Z. Tang, *Mater. Chem. Front.*, 2021, **5**, 368–374.

251 Q. Li, C. J. Zeman, G. C. Schatz and X. W. Gu, *ACS Nano*, 2021, **15**, 16095–16105.

252 R. Liu, L. Bao, S. Zhang, Z. Wu, J. Zhou, C. Liu and R. Yu, *J. Mater. Chem. B*, 2020, **8**, 11001–11009.

253 M. A. Abbas, P. V. Kamat and J. H. Bang, *ACS Energy Lett.*, 2018, **3**, 840–854.

254 K. Bharti and K. K. Sadhu, *Results Chem.*, 2022, **4**, 100288.

255 Y. Zhang, N. Feng, S. Zhou and X. Xin, *Nanoscale*, 2021, **13**, 4140–4150.

